ARTICLE   **OPEN**

Check for updates

Unraveling effects of electron correlation in two-dimensional Fe$_n$GeTe$_2$ (n = 3, 4, 5) by dynamical mean field theory

Sukanya Ghosh[1], Soheil Ershadrad[1], Vladislav Borisov[1] and Biplab Sanyal[1 ✉]

The Fe$_n$GeTe$_2$ systems are recently discovered two-dimensional van-der-Waals materials, exhibiting magnetism at room temperature. The sub-systems belonging to Fe$_n$GeTe$_2$ class are special because they show site-dependent magnetic behavior. We focus on the critical evaluation of magnetic properties and electron correlation effects in Fe$_n$GeTe$_2$ (n = 3, 4, 5) (FGT) systems performing first-principles calculations. Three different ab initio approaches have been used primarily, viz., (i) standard density functional theory (GGA), (ii) incorporating static electron correlation (GGA + U) and (iii) inclusion of dynamic electron correlation effect (GGA + DMFT). Our results show that GGA + DMFT is the more accurate technique to correctly reproduce the magnetic interactions, experimentally observed transition temperatures and electronic properties. The inaccurate values of magnetic moments, exchange interactions obtained from GGA + U make this method inapplicable for the FGT family. Correct determination of magnetic properties for this class of materials is important since they are promising candidates for spin transport and spintronic applications at room temperature.

INTRODUCTION

Magnetism and spintronics have been the topic of interest for fundamental studies as well as technological applications. Two-dimensional (2D) van der Waals (vdW) materials have recently developed increasing attention, as they are promising candidates to explore magnetism in low-dimension. Since the discovery of graphene[1], the world of two-dimensional (2D) materials is rapidly expanding to an enormous variety of systems due to their interesting properties. The discovery of intrinsic long-range magnetic order is one of the most exciting recent developments in 2D materials[2,3]. In the 2D magnetic materials spin fluctuations are expected to be strongly enhanced at finite temperature destroying long-range magnetic order according to Mermin-Wagner theorem[4]. Magnetic anisotropy reduces spin fluctuations and results in finite Curie temperature below which a magnetic order in 2D can survive and thereby lifting the restrictions imposed by Mermin-Wagner theorem[5,6]. Magnetism in 2D has started a modern era in the field of energy-efficient device fabrication due to its tunability under small or moderate-scale external perturbations[7].

The 2D magnets play a crucial role in the development of efficient spintronic devices[8] not only by size reduction but also they exhibit interesting physical phenomena stemming from 2D confinement. Prior to 2016, doping by magnetic impurities was the main strategy to induce magnetism in 2D materials, which has failed to materialize 2D magnets with high Curie temperature[9]. The exfoliation of 2D insulating ferromagnet CrI$_3$[10] and Cr$_2$Ge$_2$Te$_6$[5], in 2016, opened the doors to the application of 2D magnets in semiconducting devices.

However, the relatively low transition temperature ($T_C \approx 60$ K) intrinsic to the 2D magnetic insulators and/or semiconductors limits their utilization. On the other hand, metals exhibiting 2D magnetism are more promising for practical applications due to their high transition temperature. The most significant advantage of the metallic ferromagnets is that their conducting nature enables an interplay between spin and charge degrees of freedom, which lies at the heart of spintronics[11–13]. There are recent studies on ferromagnetic metals, such as CrTe$_x$, Cr$_2$BC, FeSe$_2$, FeTe, MnSe, and Fe$_n$GeTe$_2$, reporting high T_C (130–846 K)[14–17]. The 2D metallic Fe-Ge-Te ternary compounds or popularly known as 'FGT' systems exhibit T_C close to room temperature and gain tremendous attention due to their interesting magnetic properties[18].

Each member belonging to the FGT family exhibits a plethora of interesting physical properties, and among them, Fe$_5$GeTe$_2$ is the most complicated system. Recent experimental studies have found anomalous magnetic behavior in bulk Fe$_5$GeTe$_2$ at temperature < 100 K, which is speculated as a result of magnetostructural effects[19–21]. Recently, Liu et al., using the DFT + U approach, proposed that a competition between ferromagnetic (FM) and antiferromagnetic (AFM) coupling can give rise to a transition below 200 K in Fe$_5$GeTe$_2$, and they show the net magnetization reduces with a decrease in temperature similar to the experimental reports. However, they failed to capture the traces of this transition in Fe$_4$GeTe$_2$[22]. Though the study by Liu et al can reproduce the magnetization vs. temperature behavior of Fe$_5$GeTe$_2$, as observed in experiments, the moments of Fe atoms reported in their study are hugely overestimated (by ~1 μ_B). This suggests that the DFT + U technique cannot correctly predict the magnetic moments of Fe sublattices present in FGT systems. Similarly, other first principles studies also revealed that DFT + U is not a good approximation for the FGT systems to produce the correct lattice parameters and magnetic moments[23,24].

Electrons occupying the s and p orbitals are strongly itinerant and their kinetic energies are dominant over the Coulomb repulsion. Therefore, a static mean field approximation (like DFT) should be suitable enough to study these weakly correlated electrons. On the other hand, due to significant Coulomb interactions between electrons in the d and f orbitals, strongly correlated electrons become localized on their atomic sites. In this regime, DFT is no longer a proper approach and can yield inaccurate results. The possible solutions are DFT + U in the static

[1]Department of Physics and Astronomy, Uppsala University, Box-516, 75120 Uppsala, Sweden. ✉email: biplab.sanyal@physics.uu.se
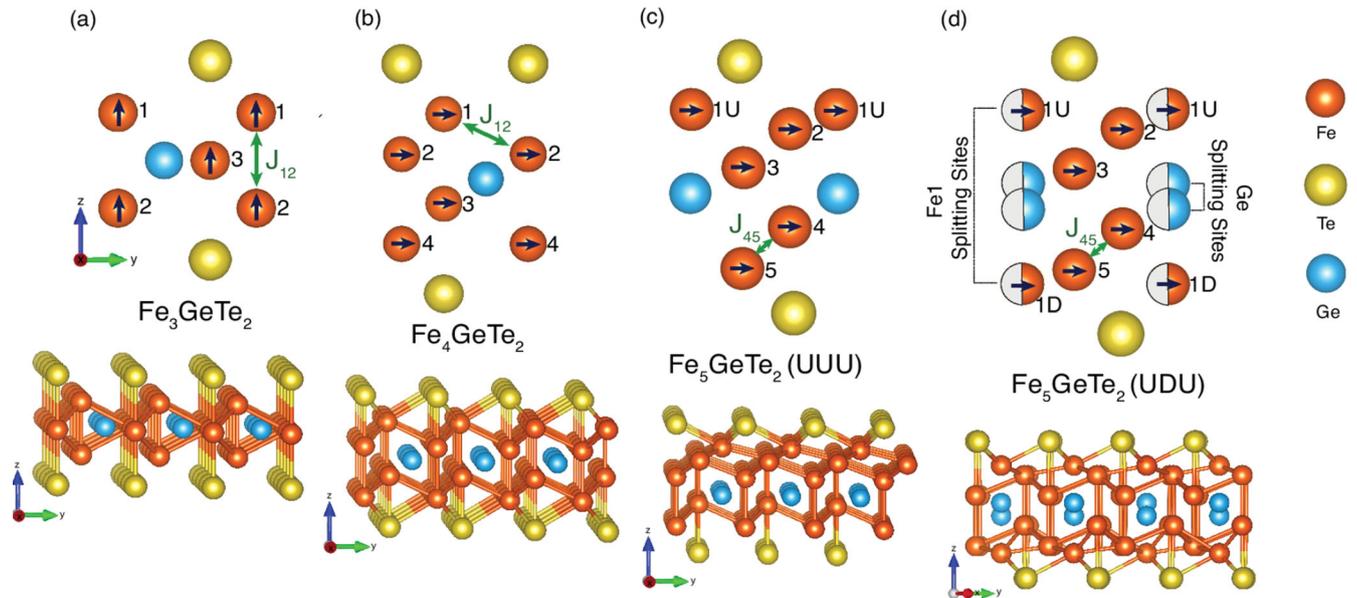
Fig. 1 Crystal structure of Fe_nGeTe_2 monolayers. Side views of **a** Fe_3GeTe_2, **b** Fe_4GeTe_2, **c** UUU Fe_5GeTe_2, and **d** UDU Fe_5GeTe_2 are side views of monolayers, where orange, yellow, and blue circles represent Fe, Te, and Ge atoms, respectively. Direction of the arrows shown inside Fe atoms, indicates the easy axis of magnetization obtained from our DFT + DMFT calculations. The half-colored circles in Fig. 1d show the Fe1-Ge split sites present in the UDU configuration. The green arrow drawn in each system shows the pair of Fe atoms exhibiting the strongest isotropic symmetric exchange interaction between each other. The lower panel shows 3D side view of Fe_nGeTe_2 monolayers.

mean field approximation, mostly applicable for Mott insulators and dynamical mean field theory with frequency-dependent self-energy for strongly correlated metals. The presence of itinerant electrons is the cause of spontaneous magnetism in 2D metals, which can be explained by the Stoner model[25]. However, in the case of metallic FGT systems, some studies show the evidence of non-Stoner magnetism where the local moments may play crucial role in the electronic and magnetic properties[26,27]. These results hint towards the possibility that the FGT systems could be an admixture of localized and itinerant electrons, exhibiting moderate electron correlation. Hence, the use of DMFT will be more justified.

The main peculiarity related to all the FGT systems is their site-dependent magnetic and electronic properties[20]. In other words, based on the magnetic moments associated with different Fe sublattices, electrons belonging to some Fe atoms are expected to have more itinerant character than others. All these complications combined together have made the proper treatment of electronic structure and magnetic behavior in FGT systems a controversial issue. Up to this date, researchers have used DFT[23,24,28], DFT + U[22] or DMFT[29,30] approaches, leaving behind the most crucial question unanswered, i.e., which method is the most reliable one to correctly treat the FGT systems. In this paper, we perform a systematic study, comparing different aspects of electronic and magnetic properties of Fe_3GeTe_2, Fe_4GeTe_2, and Fe_5GeTe_2, mostly in their 2D form (except Fe_3GeTe_2), via GGA, GGA + U, and GGA + DMFT approaches. We put forward a detailed comparative study to analyse the outcomes of these different computational techniques and their compatibility with experimental results. Since atomically thin films or monolayers of FGT systems are not experimentally studied yet, we considered the well-studied bulk Fe_3GeTe_2 as our reference to examine the accuracy of our calculations, and bridge between 3D and 2D regimes.

RESULTS AND DISCUSSION
Systems
Here we focus on the Fe_nGeTe_2 monolayers, where $n = 3, 4$ and 5, to investigate the magnetic properties of FGT systems using

different first-principles techniques, e.g., standard density functional theory (DFT), DFT with the inclusion of dynamic and static electron correlation effects.

In this section, we discuss the structural properties of the monolayers. In the case of Fe_5GeTe_2, we study both without and with the Fe1-Ge split sites, see ref. [31] for details. Figure 1 shows the side view of the Fe_nGeTe_2 monolayers, (a) $n = 3$, (b) $n = 4$, (c) $n = 5$ in UUU and (d) UDU configurations, we label each Fe atom present in the unit cell of Fe_nGeTe_2 monolayers. The lower panel in Fig. 1 shows 3D side view of the monolayers for a better clarification of the crystal structures. The space-groups (and in-plane lattice parameters) for Fe_3GeTe_2, Fe_4GeTe_2, Fe_5GeTe_2 UUU and UDU monolayers are $P\bar{6}m2$ ($a = 4.05$ Å), $P\bar{3}m1$ ($a = 3.98$ Å), $P3m1$ ($a = 3.99$ Å) and $P31m$ ($a = 7.00$Å), respectively. From the type of space-groups possessed by Fe_nGeTe_2 monolayers, it is clear that Fe_5GeTe_2 possesses lower symmetry operations, and hence less symmetric compared to $n = 3$ and 4.

Each Fe_nGeTe_2 system contains different Fe sublattices based on their structural arrangements. This sublattice classification is reflected on the electronic and magnetic properties[31,32]. In the case of Fe_3GeTe_2, Fe1 and Fe2 sublattices are equivalent, while Fe3 is different. Similarly, for Fe_4GeTe_2, Fe1 and Fe4 species belong to the same category, whereas Fe2 and Fe3 are similar.

The structural configuration for Fe_5GeTe_2 is more complex. Based on the previous experimental and theoretical studies, the Fe1 species can occupy two possible sites either above or below Ge, giving rise to Fe1-Ge split-sites[19,20,31]. Also, depending on the thermal history during the synthesis process, this system may show the absence of Fe1-Ge splitting[20,33]. To incorporate the Fe1-Ge splitting, a $\sqrt{3} \times \sqrt{3}$ cell of Fe_5GeTe_2 monolayer is constructed, where two (one) Fe1 are (is) situated above (below) Ge, this structure is referred to as 'UDU' configuration. In the absence of Fe1-Ge splitting, the Fe1 species is placed at top of the Ge atom, this structure is named as 'UUU' configuration. From our previous first-principles study, we found that the UDU configuration is energetically favored over the UUU configuration[31], resulting in the $\sqrt{3} \times \sqrt{3}$ superstructure, as already discussed by previous experimental studies[19–21,31,33]. Hence, in the following sections, we mainly focus on the UDU configuration of Fe_5GeTe_2

monolayer. All the five Fe atoms present in the unit cell of UUU configuration are different, hence this configuration is the least symmetric. In the case of UDU, we find the Fe atoms can be roughly (not strictly) categorized into four sublattices in UDU configuration: (i) Fe2, Fe5, (ii) Fe3, Fe4, (iii) Fe1U and (iv) Fe1D. The sublattice classification in Fe_nGeTe_2 systems has a direct consequence on the exchange interactions present in these systems and also the magnetization vs. temperature behavior as reported in ref. [31]. The black arrows drawn in Fig. 1a–d show the direction of the easy axis of magnetization for different Fe_nGeTe_2 monolayers obtained from our DMFT studies, which we discuss in the "Results and discussion" section.

From Fig. 1, one can see that the chemical environment, coordination number and relative position of each Fe atom w.r.t. the other Fe and Ge atoms present in the Fe_nGeTe_2 monolayers change with n. For example, in the case of Fe_3GeTe_2, the Fe1 and Fe2 atoms are situated symmetrically relative to the Ge atom with Fe1(Fe2)-Ge distance of 2.65 Å. While the Fe3 species is placed in the same z plane as Ge with a distance 2.34 Å along the xy-plane. The first nearest neighbor (NN) Fe1-Fe2 and Fe1-Fe3 distances are 2.47 and 2.65 Å, respectively. Due to this small first NN distance between Fe1 and Fe2, the strongest isotropic symmetric exchange interaction exists between the first NN of these two species, shown by the green arrow in Fig. 1a. The scenario is quite different for Fe_4GeTe_2, where the Ge atom is placed between Fe2 and Fe3 (shifted along the diagonal direction). The first NN Fe1-Fe2 (Fe4-Fe3) and Fe1-Fe3 (Fe4-Fe2) distances are 2.55 and 2.49 Å, respectively. The first NN Fe2-Ge (or Fe3-Ge) and Fe1-Ge (or Fe4-Ge) distances are 2.40 and 2.92 Å, respectively. Although the shortest first NN distance exists between Fe1 and Fe3 (Fe4 and Fe2), the highest isotropic symmetric exchange interaction takes place between Fe1 and Fe2, instead of between Fe1 and Fe3. The position of Ge atom relative to the Fe atoms is responsible for such an unexpected feature. In the case of Fe_5GeTe_2 monolayer in both UUU and UDU configurations, the most significant symmetric exchange interactions take place between the first NN Fe5 and Fe4. The exchange interactions present in different FGT monolayers are discussed in more detail in the "Results and discussion" section.

Effective Hubbard parameters

As already mentioned in the previous section, the FGT systems possess site-dependent electronic and magnetic properties. In our previous first-principles study on Fe_5GeTe_2 monolayer, we have found that though the structural properties and magnetic moments obtained using the standard DFT technique are in good agreement with the experimental reports, the calculated Curie temperature (using Monte Carlo simulations solving the Spin-Hamiltonian) is almost twice of the experimental value reported for this system[31]. This hints toward the fact that one needs to go beyond the standard DFT formalism to correctly capture the magnetic interactions. One possibility to solve such discrepancy in Curie temperature is to include the electron correlation effect in first-principles calculations which might be able to reproduce the experimental results. Here, we consider both the dynamic and static electron correlation effects and finally compare the magnetic and electronic properties obtained using GGA, LSDA, GGA + DMFT, and GGA + U techniques.

As the choice of Hubbard U parameter is always ambiguous to some extent, we have calculated the effective Hubbard U parameter (U_{eff}) for each Fe species in its magnetic ground state (as obtained from GGA) using the constrained linear response (cLR) method proposed by Cococcioni et al.[34]. This method is focused on the main effect associated with the on-site Coulomb repulsion U, neglecting the secondary effects related to the higher-multipolar terms in the Coulomb interaction. The effects of Hund's exchange interaction (J_H) are incorporated by redefining

Table 1. Effective Hubbard U parameter for Fe atoms in Fe_nGeTe_2 systems obtained from constrained linear response technique.

System	Atom	U_{eff} (eV)
Fe_3GeTe_2	Fe1	4.8
	Fe2	4.8
	Fe3	3.9
Fe_4GeTe_2	Fe1	4.5
	Fe2	4.0
	Fe3	4.0
	Fe4	4.5
Fe_5GeTe_2 (UUU)	Fe1	2.9
	Fe2	4.2
	Fe3	4.1
	Fe4	4.0
	Fe5	4.6
Fe_5GeTe_2 (UDU)	Fe1U	3.7
	Fe1D	4.0
	Fe2	4.6
	Fe3	4.1
	Fe4	4.1
	Fe5	4.6

the Hubbard U as $U_{eff} = U - J_H$ (see "Methods" for further details). The site-dependent U_{eff} values obtained using cLR for each Fe species belonging to different FGT monolayers are reported in Table 1.

There are previous reports in literature where the Fe_nGeTe_2 systems are studied considering (mostly) the static electron correlation effect, where the site-dependence of Hubbard U is not considered[30,35], except by Zhu et al., where $U = 5.5$ eV and 5.0 eV with the common $J_H = 0.8$ eV are considered for two different Fe sublattices present in Fe_3GeTe_2[29]. To the best of our knowledge, apart from our work, so far, there is no other first-principles study reporting site-dependent U value computed from either constrained linear response or any other standard computational technique (e.g., constrained random phase approximation or cRPA) generally followed for such calculations. It should be noted that the average value of U_{eff} considered by the previous authors to study any Fe_nGeTe_2 system falls in the range from 4 to 4.5 eV[29,30,35], which is close to our calculated U_{eff}^{avg} values for the Fe_nGeTe_2 monolayers. Nevertheless, it is worth mentioning that Fe_5GeTe_2 shows a much larger variation of site-dependent U values.

It is known that the size of the magnetic moment is inversely proportional to the width of the electronic density of states. The width of electronic density of states of Fe_nGeTe_2 system is ~8 eV (see Supplementary Figs. 1 and 2), and with U_{eff} ~ 4 eV, U/W ~ 0.5. Therefore, due to the existence of broad enough Fe-d bands, the Fe-d electrons are quite delocalized and the applicability of Hubbard U correction within the DFT + U formalism is questionable.

In Fe_nGeTe_2 systems, the Fe sublattices can be classified into different categories based on their magnetic properties. For example, Fe_3GeTe_2 contains two types of Fe sublattices with different magnetic moments[29,36,37], e.g., 2.18 μ_B and 1.80 μ_B based on the data obtained from neutron powder diffraction experiments[36]. From the standard DFT calculations, using GGA a the exchange-correlation functional, we find the moment of two Fe sublattices present in Fe_3GeTe_2 to be 2.49 μ_B and 1.50 μ_B. This implies that the electronic nature or localization of Fe-d states must be different for these two sublattices (see Supplementary Fig. 1 in SI). Using the cLR method we find the Fe species with

larger moment has $U_{eff} = 4.8$ eV, while for the other Fe sublattice $U_{eff} = 3.9$ eV, supporting the relationship between the degree of localization of electronic state and magnetic moment. Similarly, Fe_4GeTe_2 and Fe_5GeTe_2 systems also exhibit site dependent magnetic properties[20,30], and this feature is reflected in our calculated U_{eff}, see Table 1.

Role of electron correlation effect: comparison between DMFT, DFT, and DFT + U approaches

Within the framework of standard density functional theory, the exchange-correlation functionals (LSDA and GGA) are derived in the limit of a nearly uniform electron density, which can not correctly describe the electronic and magnetic properties of localized electronic states with strong Coulomb interactions. In some systems, the on-site Coulomb interaction (U) is quite significant and becomes much larger than the band width (W). When $U/W << 1$ the system is weakly correlated and well described by LSDA/GGA. In the case of strongly correlated regime $U/W >> 1$, which gives atomic-like behavior (e.g., Hubbard bands, Mott insulators). The most interesting case is when $U/W \sim 1$, which is a mixture of both band-like and atomic-like behavior, this can give rise to exotic phenomena like Kondo behavior, materials with heavy fermions etc.

DFT+U deals with on-site Coulomb interaction which is applicable only in the limit of $U/W >> 1$. While the dynamical mean field or DMFT covers the entire range of the parameter U/W, i.e., from uncorrelated metal to Mott insulator. Since the Fe_nGeTe_2 systems are metallic in nature, inclusion of static electron correlation or DFT + U is not supposed to be a good choice. To check the applicability of GGA + DMFT vs. GGA + U we calculate and compare the magnetic moments, exchange interactions, magnetic anisotropies and finally the Curie temperatures.

The concept of dynamical mean-field theory is to replace a lattice model with many degrees of freedom by an effective single-site model coupled to a self-consistent bath[38]. The primary quantity of DMFT is the local Green's function $G_R(z)$, defined as the one-electron Green's function projected to the correlated states at site R: $G_R(z) = P_R G(z) P_R$, where P_R is the projection operator. $G(z)$ is the one-electron Green's function, which is given by:

$$G(z) = [z + \mu - H_{eff} - \Sigma(z)]^{-1}, \qquad (1)$$

where μ is the chemical potential, the term H_{eff} is the effective Hamiltonian which includes the Hartree, exchange and correlation terms on the level of the generalized-gradient approximation (GGA). $\Sigma(z)$ is the self-energy, which goes beyond GGA and includes dynamical electronic correlations and $z = i\omega_n$ where ω_n is the Matsubara frequency. The approximation of DMFT assumes the locality of one-electron self-energy, which can be written as the sum of local self-energies for all Bravais lattice sites. In DMFT, the problem of a lattice is substituted by the impurity problem, popularly known as the effective Anderson model, where a single correlated site in the self-consistent bath is described by the bath Green's function $\mathcal{G}_0(R, z)$ defined as:

$$\mathcal{G}_0^{-1}(R, z) = G_R^{-1}(z) + \Sigma_R(z) \qquad (2)$$

Here, we perform fully charge self-consistent GGA or LSDA combined with DMFT[38] by spin-polarized T-matrix combined with fluctuating exchange approximation or SPTF solver[39], which is a perturbative solver, best suited for weak correlations, computationally less expensive, applicable for spin-polarized case treating crystal field and spin-orbit effects correctly, and gives accurate DOS and spectral densities[40]. We use site-dependent Hubbard U_{eff} parameters, obtained from the constrained linear response method, as reported in Table 1, to perform GGA + DMFT and GGA + U calculations.

In principle, DMFT is based on a mapping of lattice models onto quantum impurity models and for correlated electrons, this mapping is exact in the limit of infinite dimensions[41]. However, in recent days, DMFT has been proven to be a reliable and well-controlled

Table 2. Magnetic moments associated with each Fe atom in Fe_nGeTe_2 monolayer (computed with different techniques) in units of μ_B.

System	Species	GGA + DMFT	GGA [LSDA]	GGA+U	Expt.
Fe_3GeTe_2	Fe1	2.52	2.49 [2.33]	3.19	2.18[36]
	Fe2	2.52	2.49 [2.33]	3.19	2.18[36]
	Fe3	1.31	1.50 [1.28]	2.50	1.54[36]
	Average	2.12	2.16 [1.81]	2.96	1.62[86], 1.70[29]
Fe_4GeTe_2	Fe1	2.61	2.57 [2.41]	3.33	
	Fe2	1.58	1.75 [1.57]	2.62	
	Fe3	1.58	1.75 [1.57]	2.62	
	Fe4	2.61	2.57 [2.41]	3.33	
	Average	2.10	2.16 [1.99]	2.98	1.80[30]
Fe_5GeTe_2	Fe1U	−0.45	1.23 [1.35]	2.77	Ranges from
	Fe1D	1.76	1.71 [1.53]	3.00	0.8 to 2.5[20]
(UDU)	Fe2	2.55	2.51 [2.38]	2.97	
	Fe3	1.92	2.08 [1.91]	2.85	
	Fe4	1.85	1.98 [1.78]	2.64	
	Fe5	2.63	2.57 [2.39]	2.97	
	Average	2.05	2.42 [1.97]	3.44	1.95[87], 1.80[70]
Fe_5GeTe_2	Fe1U	−0.14	0.11 [0.00]	−2.48	Ranges from
(UUU)	Fe2	2.40	2.30 [2.22]	2.77	
	Fe3	1.95	2.04 [1.75]	2.71	
	Fe4	1.31	1.46 [1.29]	2.24	
	Fe5	2.63	2.57 [2.42]	3.29	
	Average	1.63	1.70 [1.54]	1.71	1.95[87], 1.80[70]

Values reported in square brackets are the moments obtained using LSDA. The first-principles results are obtained using GGA-optimized structures. Experimental magnetic moments are reported for the corresponding bulk Fe_nGeTe_2 systems, since experimental data are not availbale for most of the monolayer systems.

approximation to study correlation effects in bulk solids as well as for two-dimensional systems[42]. Recent studies on 2D or layered materials reported that DFT + DMFT technique describes the electronic and magnetic properties more accurately than DFT + U or standard DFT[43–45].

First, we focus on the magnetic moments calculated using GGA + DMFT, GGA, LSDA and GGA + U techniques. Table 2 reports the magnetic moment of each Fe sublattice for Fe_3GeTe_2, Fe_4GeTe_2, and Fe_5GeTe_2 (UDU configuration) monolayers (moments of Fe_5GeTe_2 in UUU configuration are reported in Supplementary Table 1 in SI). The influence of structural symmetries present in Fe_nGeTe_2 systems is reflected in the magnetic moments reported in Table 2. To investigate the magnetic and electronic properties of Fe_nGeTe_2 systems with different first-principles methods, we use the crystal structures optimized with GGA, since the unit cell parameters obtained with GGA are in better agreement with experimental values, reported in previous first-principles studies as well[23,24]. LSDA underestimates the lattice parameters by ~3% compared to experiment (see Supplementary Table 1). Therefore, we do not perform any further calculations with LSDA but with GGA. We find the values of magnetic moment obtained using GGA + DMFT and GGA are quite similar, except for the Fe1U sublattice for Fe_5GeTe_2 in UDU

configuration. It is known from previous studies that this species exhibits fluctuating moment and is mainly responsible for magnetic anomaly observed in Fe_5GeTe_2 at low temperature[19,20,31,33]. The magnetic moments of the UUU configuration are reported in Table 2. More interestingly, both the GGA + DMFT and GGA moments are close in magnitude to the moments obtained from neutron powder diffraction experiments, as we see in Table 2. There is a small discrepancy between the experimental and DMFT/DFT results which arises because the DMFT or DFT moments are calculated at 0 K for the ground state crystal structure of the monolayers, whereas the neutron powder diffraction experiments are performed at finite temperatures (~2–5 K)[20,36,37]. Note, the moment values calculated using LSDA are always underestimated compared to GGA, see Table 2, which is agreement with previous DFT studies on FGT[23,24].

In the case of GGA + U, a large deviation between the computed and experimental moments is observed. Previous DFT + U studies on FGT systems also report significant discrepancy in structural, electronic and magnetic properties of FGT systems obtained using DFT + U compared to experimental results[22–24,35,46]. Note, in the GGA+U calculations we use the fully-localized limit as the double counting (DC) correction to study the electronic and magnetic properties. We perform further calculations using the around mean field (AMF) as the DC correction using exactly the same site-dependent U_{eff} values. In that case also we find that the magnetic moments have hugely deviated from the experimental moments. This implies that GGA + U fails to reproduce the correct ground state properties of FGT systems.

Fe_nGeTe_2 systems are metallic with conducting electrons and therefore, to correctly describe the electronic properties and magnetic behavior of such metallic systems inclusion of DFT + U, i.e., consideration of on-site Coulomb repulsion is not the proper approach[23]. Instead, the dynamical electron correlation effect or DMFT may be a better choice to capture the correct electronic structure and magnetic behavior, which can properly describe the site-dependent magnetic behavior present in these systems[19,29,30]. There are recent studies on Fe_3GeTe_2 which have mentioned the existence of heavy Fermion states due to intriguing interplay between localized magnetic moments and itinerant electrons[47,48]. Also, Zhang et al. have proposed the existence of itinerant ferromagnetism in Fe_5GeTe_2.[19] These reports hint toward the fact that the electronic nature of Fe-3d states is sublattice specific. Such findings and prediction have motivated us to consider the electron correlation effect in FGT systems incorporating site-dependent U_{eff}. There are a few first-principles reports on FGT systems where the dynamical electron correlation effect is considered[29,30], but those studies do not explain why DMFT should be considered as a better technique compared to other first-principles methods, for the correct description of FGT systems. In our study, we show the importance of the dynamic electron correlation effect for the FGT systems by calculating the exchange interactions, magnetic anisotropy and more importantly the Curie temperature of these systems.

Monte Carlo simulations are performed to calculate T_C using the following spin Hamiltonian:

$$H = -\sum_{i \neq j} J_{ij} \vec{e}_i \cdot \vec{e}_j - \sum_{i \neq j} \vec{D}_{ij} \cdot (\vec{e}_i \times \vec{e}_j) - \sum_{i \neq j} K_i (e_i^z)^2, \quad (3)$$

where J_{ij} and $\vec{D}_{ij}$ are the symmetric and antisymmetric exchange interactions, respectively between the ith and jth sites. According to Eq. (3), positive (negative) sign of J_{ij} implies ferromagnetic (antiferromagnetic) interaction. K_i is the single-ion anisotropy for the ith site. In this study, we have used Heisenberg spin model which is applicable for localized moments. However, we are aware that the Fe_nGeTe_2 systems have mixed localized and itinerant character, as already speculated by previous authors[47–50]. Therefore, it would be interesting to extend the spin Hamiltonian by considering higher order exchange terms[6,51].

We first check how the J_{ij} and K_i values obtained using GGA, GGA + DMFT and GGA + U are different from each other to influence the value of T_C. We do not include the comparison of the highest magnitude of D_{ij} obtained from different methods, since the magnitude of Dzyaloshinkii-Moriya interaction (DMI) are quite small compared to the J_{ij} and MAE values, therefore DM interactions have negligible influence on T_C.

In Fig. 2 the histogram plots show (a–d) the strongest isotropic symmetric exchange interaction (J_{ij}), (e–h) magnetic anisotropy energy (MAE) and (i–l) Curie temperature (T_C) for Fe_nGeTe_2 ($n = 3, 4, 5$) systems obtained using different first-principles methods. From Fig. 2a–d we see that the sign of the highest J_{ij} interactions computed using these different methods remain unaltered but their magnitudes differ significantly. In the case of Fe_3GeTe_2 and Fe_5GeTe_2, we find the value of the strongest J_{ij} interaction obtained using GGA+DMFT is almost half of the GGA value, while this difference is even more GGA + DMFT ~ 4 times smaller than GGA) for Fe_4GeTe_2. The strongest J_{ij} value using GGA + U for $n = 3, 4,$ and 5 is overestimated by 6%, 71%, 43% (UUU) and 26% (UDU), respectively, w.r.t. the standard GGA results for the corresponding systems.

Magnetic anisotropy energy MAE = $E_\perp - E_\parallel$, calculated using different computational techniques are plotted in Fig. 2e–h, positive (negative) sign indicates in-plane (out-of-plane) easy axis. The standard DFT (both GGA and LSDA) results show that the easy axis of magnetization is strongly along the out-of-plane and in-plane directions for Fe_3GeTe_2 and Fe_5GeTe_2 monolayers, respectively, while for Fe_5GeTe_2 monolayer, MAE is weakly out-of-plane (in-plane) for the UDU (UUU) configuration. The GGA MAE results for Fe_3GeTe_2, Fe_4GeTe_2, and Fe_5GeTe_2 (UUU configuration) monolayers agree well with previous GGA results[31,31,32,52].

Next we investigate how the DFT computed MAE results get modified by the inclusion of dynamical electronic correlations. The direction of easy axis obtained using DMFT and DFT remains same for any Fe_nGeTe_2 monolayer, except for Fe_5GeTe_2 in UDU configuration. The DFT result shows weak out-of-plane anisotropy while DMFT produces small in-plane anisotropy value. The GGA + DMFT (GGA) computed MAE for Fe_3GeTe_2, Fe_4GeTe_2, Fe_5GeTe_2 in UUU and UDU configurations are: −1.51 (−1.22), 0.77 (1.01), 0.05 (0.11) and 0.02 (-0.03) meV/Fe, respectively.

It is important to note that the direction of easy axis for the Fe_3GeTe_2 and Fe_4GeTe_2 monolayers evaluated using GGA+DMFT and GGA is in good agreement with the experimental results reported for the corresponding bulk systems[30]. In the case of bulk Fe_5GeTe_2 the scenario is not so straightforward because some studies report weak in-plane easy axis[19], while some mentions canted out-of-plane[20] configuration. This can be attributed to the complexity related to the structural properties and chemical composition of Fe_5GeTe_2. Our previous first-principles study on Fe_5GeTe_2 monolayer reported that both the direction and magnitude of MAE vary depending on the concentration of Fe vacancy and the presence of Fe1-Ge split sites[31]. Since the strength of MAE for this system is quite weak, small structural changes or weak perturbations can easily tune this property.

Figure 2i–l shows the value of T_C computed using different techniques for different FGT monolayers. It is quite evident from Fig. 2i–l that T_C obtained from GGA is hugely overestimated compared with GGA + DMFT. T_C obtained using GGA is almost twice of the GGA + DMFT value for Fe_3GeTe_2 and Fe_5GeTe_2, while this difference increases in the case of Fe_4GeTe_2. The M vs. T behavior for different Fe sublattices present in the Fe_nGeTe_2 monolayers are plotted in SI.

Carefully examining Fig. 2a–d and i–l, one can see there is a direct correlation between the GGA and GGA + DMFT computed J_{ij} and T_C. For example, in the case of Fe_3GeTe_2, the value of the strongest J_{ij} coupling using GGA + DMFT and GGA are 36.52 meV/Fe and 65.32 meV/Fe, respectively. Similarly, T_C changes from 270 K (GGA+DMFT) to 480 K (GGA). A similar trend is observed
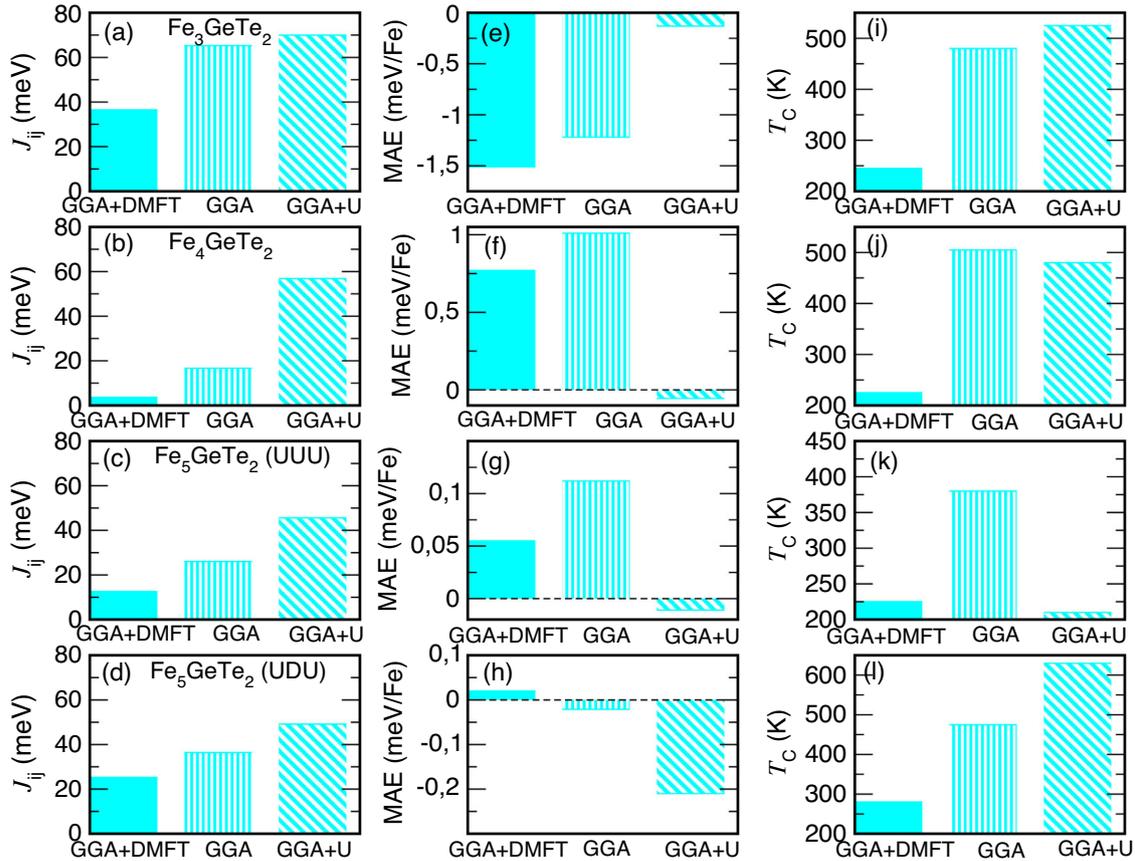
Fig. 2 J_{ij} **interactions, MAE and** T_C **for** Fe_nGeTe_2 **(n = 3, 4, 5) monolayers computed with different methods. a–d** Value of the highest J_{ij} interaction for (**a**) Fe_3GeTe_2, Fe_4GeTe_2 and Fe_5GeTe_2 (in both UUU and UDU configurations) monolayers obtained using GGA + DMFT, GGA and GGA + U. **e–h** Magnetic anisotropy energy (MAE = $E_\perp$-$E_\parallel$) Fe_3GeTe_2, Fe_4GeTe_2, and Fe_5GeTe_2 (in both UUU and UDU configurations) monolayers obtained using different computational techniques. **i–l** Curie temperature T_C for Fe_3GeTe_2, Fe_4GeTe_2, and Fe_5GeTe_2 (in both UUU and UDU configurations) monolayers.

between the highest J_{ij} and T_C for Fe_5GeTe_2 monolayer in UDU configuration as well. In the case of Fe_4GeTe_2, although the highest J_{ij}(GGA + U) is almost three times larger than J_{ij}(GGA), GGA + U gives significant antiferromagnetic J_{ij} interactions, which are ~10 times stronger than GGA. The presence of significant antiferromagnetic components in J_{ij} causes a small reduction in T_C(GGA + U) compared to T_C(GGA). Supplementary Fig. 4 shows the difference between J_{ij} interactions obtained from GGA and GGA+U. Using the J_{ij} values calculated from different first-principles approaches, the following trend is observed for Fe_4GeTe_2 monolayer: T_C(GGA) > T_C(GGA + U) > T_C(GGA + DMFT). From this discussion, it is clear that distant neighbor interactions also play an important role in determining the T_C in these 2D metallic systems especially the antiferromagnetic interactions (Supplementary Figs. 4 and 8) present for a number of second nearest neighbors. These results establish the fact that, T_C of Fe_nGeTe_2 monolayers are primarily influenced by the overall J_{ij} or isotropic symmetric exchange interactions present in the system, i.e., $\sum_{i \neq j} J_{ij}$, the first term in Eq. (3).

The T_C results reported in Fig. 2 are obtained without considering site-dependent MAE for different Fe sublattices present in Fe_nGeTe_2 monolayers. To test the validity of this approximation, we have calculated MAE for different Fe sub-lattices present in Fe_3GeTe_2 and Fe_4GeTe_2 monolayers using magnetic-force theorem[53]. We re-calculate T_C using site-dependent MAE values and find that the obtained T_C values are very similar to the previous ones. For example, in the case of Fe_3GeTe_2 monolayer, MAE varies by 5% between two types of Fe

sites. Site-dependent and -independent anisotropy energies cause only ~2% difference in the calculated T_C. For Fe_4GeTe_2 monolayer, difference in MAE between two Fe sites is 8%, which causes ~1.5% change in T_C.

Moreover, we also observe that the Monte Carlo simulations performed with and without single-ion anisotropy show a negligible difference in T_C for Fe_nGeTe_2 monolayer, see Supplementary Fig. 13 in SI. This can be related to the discussions in a recent paper[54] where it was demonstrated that the short-ranged isotropic exchange interactions for finite-sized cells used in Monte Carlo simulations may establish a magnetic order at a finite temperature without any magnetic anisotropy.

It is important to note that, the value of T_C for Fe_nGeTe_2 monolayers obtained using GGA + DMFT fall in the same range as reported in the experiments on few-layer thick or bulk FGT systems. Since in the bulk FGT systems, monolayers are stacked together via weak vdW forces, a single monolayer could be considered as a reasonable representative of the bulk, though the interlayer interactions are absent in this case. Therefore, T_C(GGA + DMFT) obtained for monolayers should be compatible with their bulk counterpart. T_C for monolayer (bulk) Fe_3GeTe_2, Fe_4GeTe_2 and Fe_5GeTe_2 (UDU configuration) systems obtained from GGA+DMFT (experiments) are the following: 245 K (220 K[29,30]), 225 K (270 K[30]) and 280 K (275–310 K[19,20,55]), respectively. From these values of T_C we see there is no linear relationship as a function of n for different FGT monolayers, while the T_C values reported in experiments show the linear trend for bulk FGT systems[19]. Even in the case of GGA+DMFT, there is still some overestimation of T_C

obtained for monolayer Fe_3GeTe_2 compared to the experimental values (126 K–140 K) reported for this system[56,57]. Such mismatch may arise due to the presence of Fe-vacancies or defects in the real sample, which can alter the exchange interactions and hence the T_C[58]. For example, studies on bulk Fe_3GeTe_2 show T_C can vary from 220 K to 160 K depending on the concentration of Fe (as well as Ge and Te) atoms present in the sample[36,59].

Therefore, one may conclude that the standard GGA technique gives reasonable results for magnetic moment and MAE, but overestimates the exchange interactions, especially the isotropic symmetric exchange, hence, leads to high values of the Curie temperature T_C. While the magnetic moments, magnetic anisotropy energy and Curie temperature computed using GGA + DMFT are in a good agreement with the experimental studies reported in literature. The outcome from GGA + U calculations, for example, the magnetic moment, MAE and T_C are not at all compatible with experimental results. Therefore, the consideration of static electron correlation (in the limit of $U/W \gg 1$) can not be a reasonable choice for the correct description of the electronic and magnetic properties of FGT systems.

Besides comparing the Curie temperature with experiments, we evaluate the electronic properties, e.g., density of states, spectral function, effective mass and Sommerfeld co-efficient to judge the suitability of different first-principles methods, as discussed in the "Results and discussion" section.

Interatomic exchange interactions

Based on our results discussed in the "Results and discussion" section, we find that DMFT produces a reasonable outcome in terms of the magnetic properties of FGT monolayers. In this section, we discuss the isotropic symmetric and antisymmetric exchange interactions computed with the inclusion of dynamical electronic correlation effects. We focus on the exchange interactions obtained using DMFT, because, as discussed in the "Results and discussion" section, this technique captures the physical (electronic and magnetic) properties of FGT systems more accurately than other methods. It should be noted that we have followed the standard approach of calculating the parameters of the spin Hamiltonian for the ground state structure at $T = 0$ K and using them in Monte Carlo simulations. It is interesting to note that some recent experimental studies have reported modifications in crystal structure as a function of temperature[20,59,60] and this may have an important consequence in magnetic properties. This topic will be considered in a future study.

Isotropic symmetric exchange parameters

The isotropic symmetric exchange interactions J_{ij} within the GGA +DMFT framework is given by[61]:

$$J_{ij} = \frac{T}{4} \sum_n \mathrm{Tr}[\Delta_i(i\omega_n)G_{ij}^{\uparrow}(i\omega_n)\Delta_j(i\omega_n)G_{ji}^{\downarrow}(i\omega_n)], \quad (4)$$

where the trace is over the orbital degrees of freedom, T is the temperature, and ω_n is the nth Matsubara frequency, G_{ij} is the intersite Green's function between sites i and j. Therefore, according to Eq. (4), the exchange interactions J_{ij} depend on the onsite exchange splitting Δ_i and intersite Green's function G_{ij}. The onsite exchange splitting term Δ_i which includes the self-energy is given by:

$$\Delta_i(i\omega_n) = H_{KS}^{\uparrow} + \Sigma_i^{\uparrow}(i\omega_n) - H_{KS}^{\downarrow} - \Sigma_i^{\downarrow}(i\omega_n), \quad (5)$$

where H_{KS} and Σ_i are the Kohn-Sham Hamiltonian and site-dependent self-energy. The self-energy is obtained by solving the DMFT equations. In DMFT calculations, the self-energy is frequency-dependent, which is also true for the exchange splitting. Though the self-energy Σ is a single-site quantity, it affects the intersite Green's function according to Eq. (1)[61]. J_{ij}

parameters for each Fe sublattice in Fe_nGeTe_2 ($n = 3, 4, 5$) systems obtained using DMFT are plotted in Fig. 3.

Figure 3a, b shows the J_{ij} interactions obtained using when $i =$ Fe1 and Fe3 for Fe_3GeTe_2 monolayer as a function of the nearest neighbor distance R_{ij} (normalized by the lattice parameter a). The dominating exchange interaction is ferromagnetic (FM) between different types of Fe species, i.e., when $i \neq j$ while for $i = j$, the first NN interaction is antiferromagnetic (AFM) irrespective of the type of Fe sublattice. As already mentioned, the first NN distance between Fe1 and Fe2 is smaller than the first NN Fe1-Fe3 distance, therefore, as expected, the strongest FM J_{ij} interaction takes place between the first NN Fe1-Fe2 pair, see Fig. 3a, b. From the orbital decomposition of J_{ij} interactions (see Supplementary Table 1), we find the dominating contribution to the first nearest neighbor (NN) J_{12} interaction comes from the d_{z^2} orbital of the vertically aligned Fe1 and Fe2 atoms, see Fig. 1a.

The J_{ij} values calculated using standard GGA, GGA + DMFT and GGA + U techniques for Fe_3GeTe_2 monolayer are plotted in Supplementary Fig. 3. This comparison clearly shows that, although the sign of J_{ij} interactions remains unchanged, their magnitude differs drastically, which in turn modifies the T_C. Figure 3a–b shows the largest isotropic symmetric exchange interaction takes place between Fe1 and Fe2. Fe-d orbital resolved J_{ij} interactions for Fe_3GeTe_2 monolayer reported in Supplementary Table 2 show the major contribution to J_{12} comes from Fe-d_{z^2} state. Inclusion of dynamical electron correlation significantly modifies this particular interaction. We check the robustness of GGA+DMFT method with respect to the correlation strength by calculating the J_{ij} interactions for different $U_{eff} = U - J$ values using GGA + DMFT, for example, $U = 5.0$ eV and $J_H = 1.2$ eV, Seo et. al. considered these values in their studies on Fe_nGeTe_2 systems[30]. Our results show the maximum deviation in the largest J_{ij} value is ~8% between the site-dependent U_{eff} values (calculated from cLR method) and $U = 5.0, J_H = 1.2$ eV, for Fe_3GeTe_2 monolayer, see Supplementary Fig. 4.

The J_{ij} interactions obtained using GGA+DMFT for $i =$ Fe1 and Fe2 of Fe_4GeTe_2 monolayer are plotted in Fig. 3c, d, respectively. Supplementary Fig. 5 shows the isotropic exchange interactions of Fe_4GeTe_2 computed using GGA, GGA + DMFT and GGA + U. Similar to Fe_3GeTe_2, in the case of Fe_4GeTe_2 also, the sign of J_{ij} couplings remain unchanged irrespective of the type of computational technique. The J_{ij} interactions are mostly FM in this system and dominating FM interaction takes place between Fe1-Fe2 and Fe3-Fe4.

The nature of J_{ij} interactions is relatively complicated in the case of Fe_5GeTe_2. The dominating exchange interaction between different Fe sublattices is FM for $i = 2, 3, 4$ and 5, while a small AFM coupling exists between the same Fe species, see Fig. 3g–j. This scenario is quite different for $i = 1U$ and 1D, where significant AFM interactions are present even for $i \neq j$, i.e., between 1U or 1D and other Fe species, see Fig. 3e, f. The presence of such non-negligible AFM coupling implies the existence of exchange frustration in Fe_5GeTe_2. Supplementary Fig. 6 shows how the absence and presence of electron correlation affect the J_{ij} interactions present in Fe_5GeTe_2 for the UDU configuration. The J_{ij} interactions computed using GGA and GGA + U in the UDU configuration are plotted in Supplementary Fig. 7.

Using the DMFT computed J_{ij} values we calculate exchange stiffness constant A for the Fe_nGeTe_2 monolayers, which is given by:

$$A = \frac{1}{2V} \lim_{\kappa \to 0} \sum_{i \neq j} J_{ij} R_{ij}^2 e^{-\kappa R_{ij}} \quad (6)$$

where V is the unit cell volume per magnetic site and κ is the damping parameter. The term $e^{-\kappa R_{ij}}$ is introduced to improve the convergence of A with the cutoff radii or R_{ij}[62]. We check the dependence of A as a function of κ for different R_{ij} varying κ from 0 to 2 and we find for $\kappa \geq 0.5$ different curves coincide. Using those
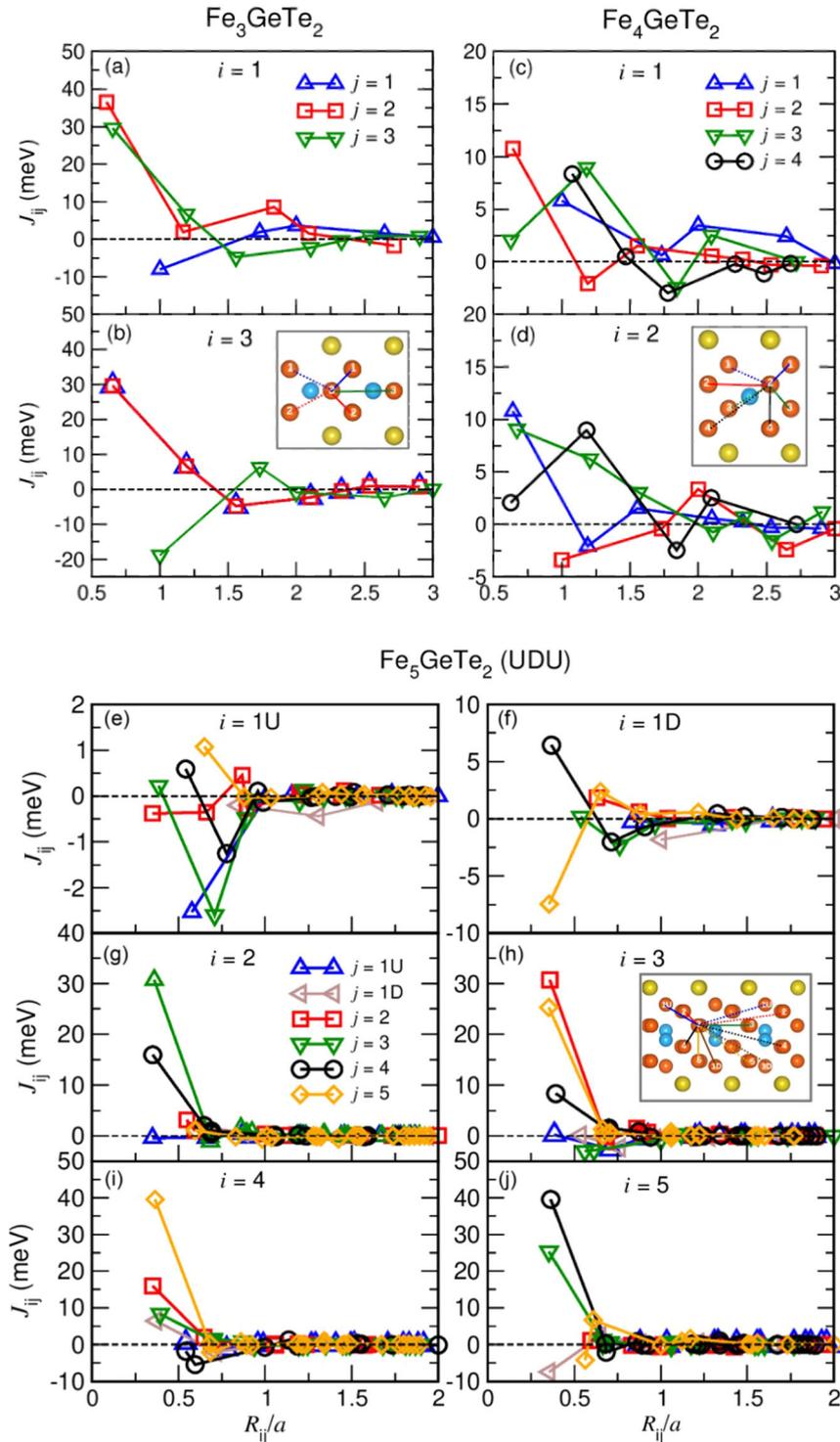
Fig. 3 **Distance dependent isotropic symmetric exchange parameters.** Isotropic symmetric exchange parameters J_{ij} as a function of neighboring distance R_{ij} for **a, b** Fe_3GeTe_2, **c, d** Fe_4GeTe_2 and **e–j** Fe_5GeTe_2 monolayer, obtained using GGA + DMFT. The J_{ij} values reported here are multiplied by the corresponding coordination numbers.

results we fit the exponential function $f(\kappa) = ae^{-b\kappa} + c$ and calculated $f(0)$ at the $\kappa = 0$ limit. The stiffness constant A is estimated this way. Since we are interested in monolayer FGT systems, Eq. (7) is modified in the following way:

$$A = \frac{1}{2S}\lim_{\kappa \to 0}\sum_{i \neq j} J_{ij}R_{ij}^2 e^{-\kappa R_{ij}} \tag{7}$$

where S is the unit cell area. The exchange stiffness constants A for Fe_nGeTe_2 monolayers calculated using Eq. (7) are given by: 4.63 meV ($n = 3$), 4.30 meV ($n = 4$), 3.24 meV ($n = 5$, UUU) and 13.88 meV ($n = 5$, UDU).

Next, we study the antisymmetric exchange (D_{ij}) interactions. The D_{ij} interactions are calculated using the relativistic generalization of the Lichtenstein-Katsnelson-Antropov-Gubanov (LKAG)
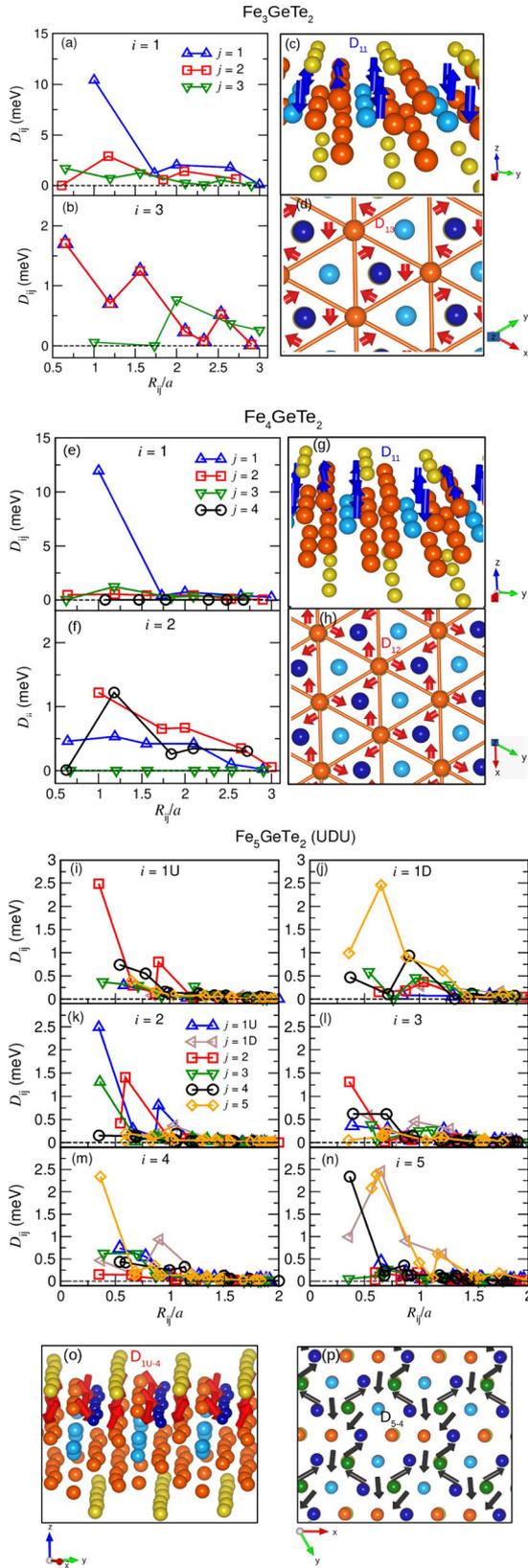
Fig. 4 Distance dependent anisotropic exchange parameters.
Antisymmetric exchange parameters $D_{ij} = \sqrt{D_{x_{ij}}^2 + D_{y_{ij}}^2 + D_{z_{ij}}^2}$ as a function of neighboring distance R_{ij} for **a, b** Fe_3GeTe_2, **e, f** Fe_4GeTe_2 and **i–n** Fe_5GeTe_2 monolayer, obtained using GGA+DMFT. **c, d, g, h, o, p** The first neighbor DM interactions between different ith and jth pairs. The D_{ij} values are multiplied by the corresponding coordination numbers.

components. The 3×3 tensor with only the antisymmetric terms is the following: $\begin{pmatrix} 0 & D_{ij}^z & -D_{ij}^y \\ -D_{ij}^z & 0 & D_{ij}^x \\ D_{ij}^y & -D_{ij}^x & 0 \end{pmatrix}$, where, $D_{ij}^z = \frac{1}{2}(J_{ij}^{xy} - J_{ij}^{yx})$

Figure 4 shows the antisymmetric exchange interactions or Dzyaloshinkii-Moriya interaction (DMI) $D_{ij} = \sqrt{(D_{ij}^x)^2 + (D_{ij}^y)^2 + (D_{ij}^z)^2}$ between different ith and jth Fe sites present in Fe_nGeTe_2 monolayers, computed using GGA+DMFT. The DM interactions for the two different Fe sublattices (Fe1 and Fe3) of Fe_3GeTe_2 are plotted in Fig. 4a, b. The strongest D_{ij} interaction takes place between Fe1-Fe1, i.e., Fe atoms situated in the same z plane, as we see in Fig. 4a the first nearest neighbor D_{11} interaction is ~ 10 meV. Figure 4c shows the side view of the first nearest neighbor D_{11} acting between Fe1-Fe1 and the dominating contribution comes from the D_z component. The next significant DM interaction takes place between the first nearest neighbors Fe1 and Fe3. The inversion symmetry is broken locally for the bonds where we find a non-zero DM interaction. As an example, a significant magnitude of first-nearest neighbor (NN) D_{11} interaction exists due to the absence of inversion center between Fe1-Fe1 neighbors. Relative to the center of the Fe-Fe bond, the local atomic environment is asymmetric due to the presence of Ge and Te ions below and above the Fe plane, respectively. The first NN DMI is zero between Fe1 and Fe2, due to the presence of inversion center between Fe1 and Fe2 bond.

Figure 4d shows the top view of the DM interaction vectors between Fe1 and Fe3 sites, which have mainly the in-plane components (D_x and D_y). It is important to note that the D_{11}^z as well as the D_{13}^x and D_{13}^y vectors present in the unit cell almost cancel each other due to the structural symmetry of this system. More interestingly, the first nearest neighbor (NN) D_{13} interaction is essentially zero, this happens because the NN Fe1 and Fe2 atoms are inversion symmetric partners with respect to the z axis, see Fig. 1a. Comparing between the magnitudes of the highest D_{ij} and J_{ij} values of Fe_3GeTe_2 monolayer, we see the DM interaction is ~3 times smaller than the isotropic symmetric exchange interactions. Supplementary Fig. 9 shows the DM interactions present in Fe_3GeTe_2 obtained using GGA and GGA + DMFT.

The D_{ij} interactions for different Fe sublattices of Fe_4GeTe_2 are plotted in Fig. 4e, f. Similar to Fe_3GeTe_2, in this case also the first NN D_{11} interaction (between Fe1 and Fe1) has the highest contribution to DMI in Fe_4GeTe_2 with D_z as the dominating component, see Fig. 4g. The next dominating DM interaction takes place between the first NN Fe2-Fe2 pair, and the direction of D_{22} is mainly along z. There exists non-zero DMI between Fe1-Fe2 or Fe3-Fe4 where the in-plane components dominate, see Fig. 4h. The first nearest neighbor D_{13} or D_{24} interaction is zero, while the long-range D_{13} (or D_{24}) are non-zero. More interestingly, DM interactions do not exist between Fe1 and Fe4 (Fe2 and Fe3), due to the presence of inversion centre along the bonds formed between Fe1 and Fe4 (Fe2 and Fe3). Hence, these Fe sites are inversion symmetric partners, see Fig. 1b. The DM interaction vectors between different Fe-sublattices of Fe_4GeTe_2 are plotted in Fig. 4g, h. Supplementary Fig. 10 shows the DM interactions present in Fe_4GeTe_2 obtained using GGA and GGA + DMFT.

Figure 4i–n show the DM interactions for different Fe sublattices of Fe_5GeTe_2 in the UDU configuration. The D_{ij} interactions are quite complex in this case compared to the Fe_3GeTe_2 and

formula[63]. In the fully relativistic limit, the magnetic exchange parameters are (3×3) tensors, with the isotropic exchange terms J_{ij} as the diagonal components and the antisymmetric DM and the symmetric anisotropic exchange interactions in the off-diagonal
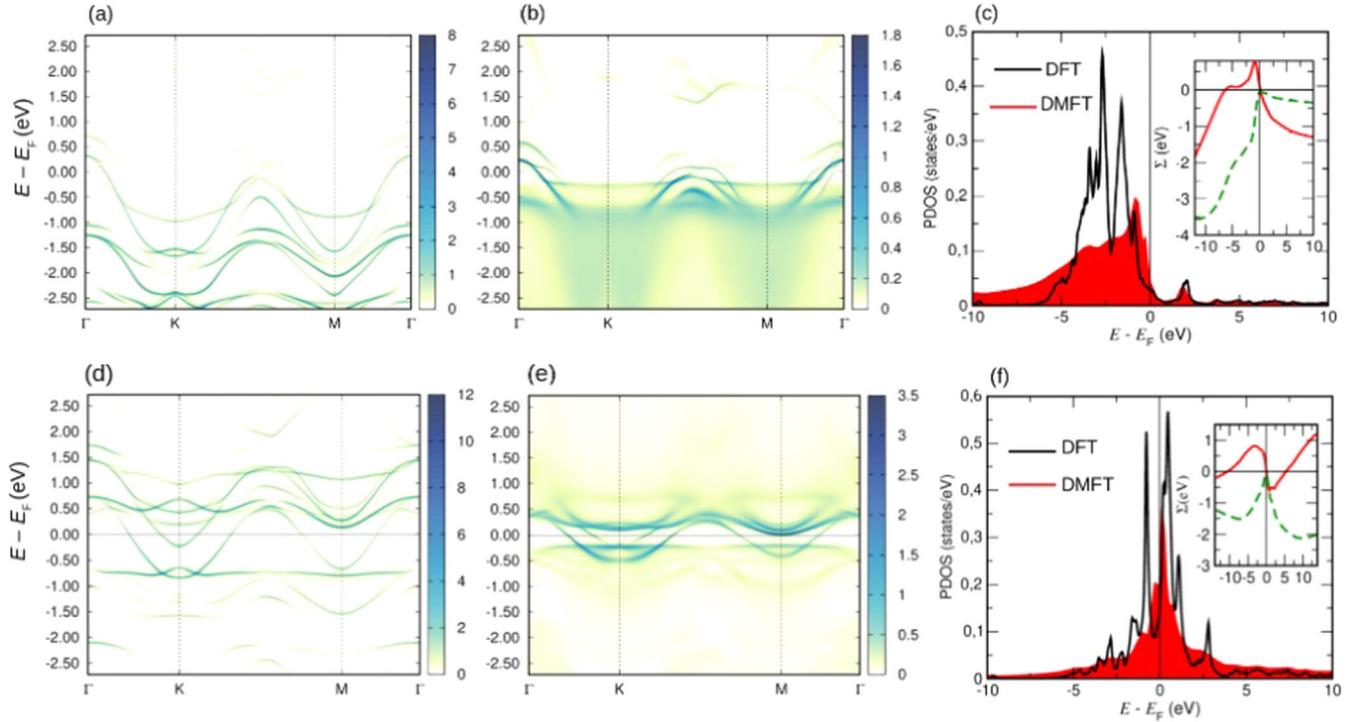
Fig. 5 Comparison of spectral properties of Fe₃GeTe₂ monolayer. Band structure projecting on both spin channels of d_{z^2} orbital for Fe1 (Fe2) in Fe₃GeTe₂ using **a, d** GGA and **b, e** GGA+DMFT. **c, f** show the GGA (black) vs. GGA+DMFT (red) density of states projected on d_{z^2} orbital of Fe1(Fe2) for both spin channels. Insets in (**c**) and (**f**) show the real (red solid) and imaginary (green dashed) parts of the self-energy Σ for both spin channels.

Fe₄GeTe₂ monolayers, because this system is less symmetric than the first two FGT systems. The inversion centre does not exist along any of the bonds formed between different Fe atoms. Figure 4o, p shows the DM vectors between Fe1U-Fe4 and Fe4-Fe5 pairs in Fe₅GeTe₂. Supplementary Fig. 11 shows the DM interactions present in Fe₅GeTe₂ monolayer in the UUU configuration computed using GGA and GGA + DMFT.

Though the scalar form of D_{ij} interactions plotted in Fig. 4 shows a non-zero contribution for some of the site neighbors, the net DMI for all the nearest neighbors of a given site i is quite small due to the structural symmetries present in the pristine FGT monolayers. Using the computed $\vec{D}_{ij}$ values we calculate the spiralization constant D for the Fe$_n$GeTe₂ monolayers defined as:

$$D = \frac{1}{S} \lim_{\kappa \to 0} \sum_{i \neq j} \vec{D}_{ij} \otimes \vec{R}_{ij} e^{-\kappa R_{ij}} \qquad (8)$$

In this case D is 3×3 tensor. Since our system of interest is 2D FGT systems, we divide Eq. (8) by the unit cell area S (same as Eq. (7)).

The spiralization constants calculated from the DM vectors are negligible in the case of Fe₃GeTe₂ and Fe₄GeTe₂, because the net DM vector acting between any sites i and j gets significantly canceled out due to the structural symmetries, as we see in Fig. 4c, d, g, h. In the case of Fe₅GeTe₂ in UUU and UDU configurations, the diagonal terms in Eq. (8) are very small but there are some non-negligible off-diagonal terms. The highest off-diagonal term of the spiralization tensor for UUU and UDU configurations are 0.04 and 0.031 meV Å⁻¹, respectively. Due to the existence of such small DM interactions in Fe$_n$GeTe₂ monolayers, there is a negligible contribution to T_C from the antisymmetric exchange interactions.

Electronic structure

In order to investigate how electron correlation effect modifies the electronic structure we compare the band structure and

k-resolved spectral density obtained from GGA + DMFT, along the high symmetry directions. We also discuss the difference in density of states for these two cases.

The DMFT expressions for spectral density $S(\mathbf{k}, \epsilon)$ and density of states (DOS) $D(\epsilon)$ are given by:

$$S(\mathbf{k}, \epsilon) = -\frac{1}{\pi} \sum_{\chi} <\mathbf{k}, \chi| \text{Im} G(\epsilon + i0) |\mathbf{k}, \chi>, \qquad (9)$$

$$D(\epsilon) = -\frac{1}{\pi} \text{Tr}[\text{Im} G(\epsilon + i0)], \qquad (10)$$

Among the three Fe$_n$GeTe₂ systems, $n = 3$ is the simplest one and the J_{ij} interactions present in this system are less complicated. Hence, we focus only on Fe₃GeTe₂, to see the change in electronic structure due to dynamical electronic correlations. Here we focus on Fe1-d_{z^2} state since from the orbital resolved analysis of J_{ij} interactions we see this particular orbital of Fe1 (and/or Fe2) has dominating contribution to the isotropic symmetric exchange interaction J_{12} (between Fe1 and Fe2), as reported in the "Results and discussion" section and Supplementary Table 2. Figure 5 shows the comparison of electronic structures of Fe₃GeTe₂ monolayer obtained without and with dynamical correlations.

The spin-polarized GGA and GGA + DMFT band structures for Fe1 (or Fe2) sublattice of Fe₃GeTe₂ projecting on d_{z^2} orbital are plotted along the high-symmetry directions in Fig. 5a–b (up spin) and d–e (down spin), respectively. The GGA band structure contains sharp energy bands, while the DMFT bands are smeared out due to the finite quasiparticle lifetime[40] induced by a non-zero imaginary part of the self-energy. Furthermore, the energy levels are shifted towards the Fermi level, which is attributed to the real part of the self-energy, and become more flat due to correlations. Correlations also reduce the bandwidth in the momentum-resolved spectral function $S(k, \epsilon)$. In Fig. 3a we see the first NN J_{12}, i.e., the isotropic symmetric exchange interaction between Fe1

and Fe2, is the strongest among all J_{ij} interactions present in this system. The orbital decomposed results show the first NN Fe1 and Fe2 atoms interact mainly via their d_{z^2} orbitals. Due to this reason, here we focus on the d_{z^2} orbital of one of these Fe species, and compare its electronic nature using GGA and GGA + DMFT. Comparing between the GGA and GGA+DMFT band structures we find the narrowing or shift of bands towards the Fermi energy is quite significant along $\Gamma - K$ and $\Gamma - M$ directions for the spin-up and down channels, respectively.

The GGA (black) and GGA+DMFT (red) density of states $D(\epsilon)$ projecting on Fe1 (or Fe2) d_{z^2} orbital for both spin channels are plotted in Fig. 5c, f. It follows from Fig. 5c, f that DMFT causes noticeable renormalization of Fe1-$3d_{z^2}$ projected density of states (PDOS). In the case of spin-up channel of the DMFT PDOS (red curve), the first peak is situated closer to the Fermi energy compared to the GGA PDOS, see Fig. 5c. Similarly, for the spin-down channel the electronic states are also shifted toward the Fermi level for DMFT PDOS, see Fig. 5f.

Even though the integration of spin-polarized DOS up to the Fermi energy remains almost the same for both DFT and DMFT, (which causes similar value of magnetic moments for DFT and DMFT), the electronic spectra gets modified upon the inclusion of dynamical electronic correlations. These modifications in the PDOS can be understood by analyzing the real (red solid) and imaginary (green dashed) parts of the self-energy Σ, displayed as the insets in Fig. 5c, f, for the up and down spin channels, respectively. According to Eq. (10) the GGA+DMFT DOS contains imaginary part of the Green's function, and the self energy term Σ is included in the denominator of Green's function, see Eq. (1). The quasiparticle energies are renormalized by the real part of the self-energy which shifts the positions of the peaks in the DMFT spectrum. The high and positive value of the self-energy for the up and down spin channels within the energy range between 0 and −5 eV shifts the spectrum toward the Fermi level. The imaginary part of the self-energy causes broadening of the peaks present in PDOS, leading to an effective decrease of their intensities. Note, the imaginary part of the self energy is ~0 at and close to the Fermi energy, implying the quasi-particles have longer lifetimes, according to Fermi liquid theory.

The difference in electronic structure between GGA and GGA + DMFT, displayed in Fig. 5, is responsible to modify the isotropic symmetric exchange interactions present in Fe$_3$GeTe$_2$ monolayer, which in turn changes the Curie temperature. The band structure plot along high-symmetry directions shows that the energy levels get more localized in the case of GGA + DMFT than GGA, thus the dynamical correlations reduce the electron

hopping amplitude between different sites and consequently the intersite Green's-function G_{ij} in Eq. (4). Therefore, the isotropic symmetric exchange interactions present in FGT systems get significantly reduced in DMFT leading to smaller values of T_C.

Discussion on bulk FGT systems

T_C obtained from our Monte Carlo simulations for Fe$_3$GeTe$_2$, Fe$_4$GeTe$_2$ and Fe$_5$GeTe$_2$ (UDU configuration) monolayers are 275 K, 220 K and 280 K, respectively. From these results one can see that T_C does not increase linearly as a function of $n(=3, 4,$ and $5)$, which is in contrast to previous studies on bulk Fe$_n$GeTe$_2$ systems[19,30]. This implies some important features must be missing in the case of FGT monolayers compared to the bulk FGT systems. Due to the lack of those features, the expected T_C vs. n relationship is not observed.

To understand the magnetic and electronic properties of bulk FGT systems we focus on bulk Fe$_3$GeTe$_2$ since this is the simplest member and experimental results are reported mainly for this particular system so far. Based on our (DFT and DFT+DMFT) results we find (as mentioned in the "Results and discussion" section) that the value of T_C primarily depends on J_{ij}. Therefore, the sign and magnitude of J_{ij} interactions present in bulk Fe$_3$GeTe$_2$ should be the main features to tune the T_C from monolayer to bulk (or vice versa). We calculate the magnetic exchange interactions and T_C for bulk Fe$_3$GeTe$_2$. Our results show both the strength and magnitude of intralayer J_{ij} interactions remain almost the same for monolayer and bulk, see Supplementary Fig. 14. Therefore the intralayer J_{ij} interactions do not play any role in modifying the T_C for this system.

Next, we focus on the interlayer symmetric exchange interactions considering ferromagnetic intra and interlayer spin configuration. Our GGA + DMFT results show that significant antiferromagnetic (AFM) couplings exist in bulk Fe$_3$GeTe$_2$, as already discussed in the literature[60,64,65]. Figure 6a–c shows the side view of bulk Fe$_3$GeTe$_2$ and the interlayer symmetric exchange interactions J_{ij} for $i = 1$ and $i = 3$, respectively. Bulk Fe$_3$GeTe$_2$ has the vdW gap of 3.47 Å and the out-of-plane lattice constant is 16.33 Å. Note, the unit cell of bulk Fe$_4$GeTe$_2$ and Fe$_5$GeTe$_2$ contain three formula units along z direction with thickness 29.08 and 29.20 Å, respectively[20,30]. Figure 6b, c significant interlayer AFM interactions are present in bulk Fe$_3$GeTe$_2$. Though these interlayer J_{ij} interactions are weaker than the intralayer interactions, such exchange couplings are enough to tune the T_C. As a result, the Curie temperature changes from 260 K (monolayer) to 205 K (bulk), and this value of T_C for the pristine bulk Fe$_3$GeTe$_2$ is in good agreement with the previously reported experimental
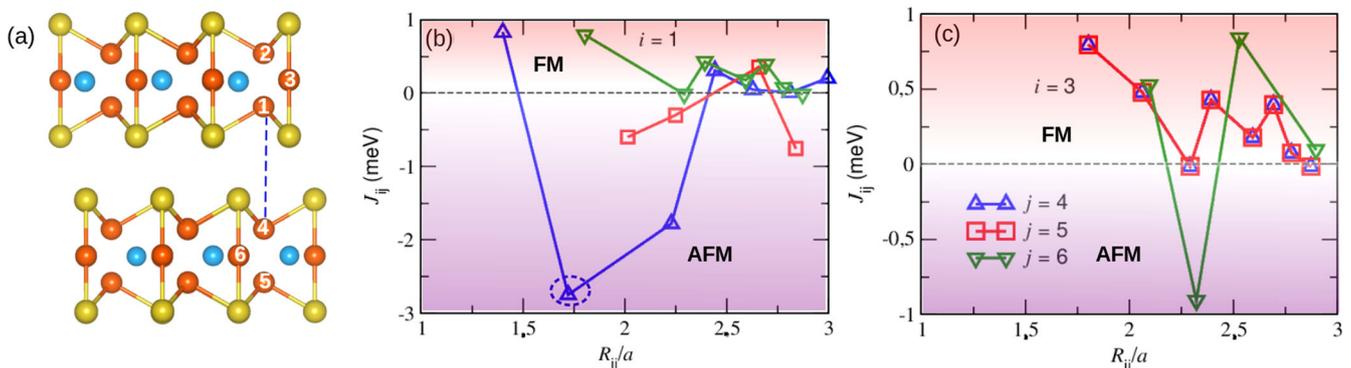

Fig. 6 Crystal structure and J_{ij} interactions of bulk Fe$_3$GeTe$_2$. a Side view of bulk Fe$_3$GeTe$_2$, the sublatiices highlighted in white show the strongest AFM interaction. Interlayer symmetric exchange couplings J_{ij} as a function of neighboring distance R_{ij} for Fe$_3$GeTe$_2$ bulk for the ith site as (**b**) Fe1 and (**c**) Fe3. These results are obtained using GGA+DMFT. The second nearest neighbor J_{14} (or J_{36}) interaction shows significant AFM coupling. The exchange parameters are multiplied by the corresponding coordination numbers. The blue dashed line in (**a**) between Fe1 and Fe4 shows the Fe sublattices taking part into the highest AFM interaction, highlighted by the blue circle in (**b**).
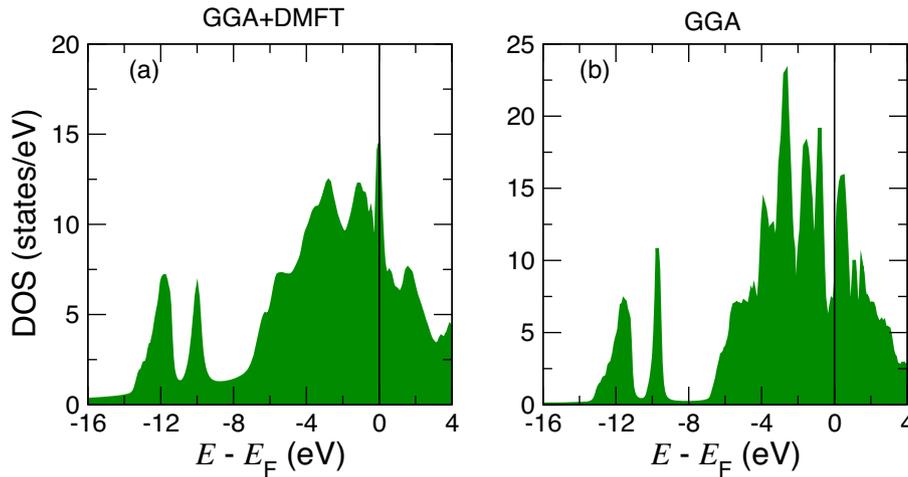
Fig. 7 **Density of states $D(\epsilon)$ of Fe_3GeTe_2 bulk.** $D(\epsilon)$ calculated using (**a**) GGA+DMFT (with SPTF solver at $T = 150$ K) and (**b**) GGA.

findings[30,36,37,48,57,59] and computed values of T_C[30,66]. Note, the MC simulations are performed solving the spin Hamiltonian considering intra and interlayer FM spin configurations in bulk Fe_3GeTe_2. The value of T_C obtained from standard GGA calculations for bulk Fe_3GeTe_2 is found to be 410 K, which is hugely overestimated compared to GGA + DMFT and also w.r.t. the experimental transition temperature. Supplementary Fig. 15 shows the comparison in magnetization (M) vs. temperature (T) behavior for bulk Fe_3GeTe_2 between GGA and GGA + DMFT.

Similar to Fe_3GeTe_2, if we compute T_C of bulk Fe_4GeTe_2 and Fe_5GeTe_2 (UDU configuration), then we should in principle obtain the linear relationship between T_C and n ($n = 3, 4, 5$). Since we have already discussed in this study that DFT + DMFT describes the physical properties of FGT systems more accurately than standard DFT or DFT + U, therefore one has to perform DFT + DMFT calculations for bulk Fe_4GeTe_2 and Fe_5GeTe_2 to get compatible results with experiment. But these DMFT calculations are computationally expensive due to a large number of atoms. Therefore, in this study, we have limited ourselves to DFT + DMFT calculations only for bulk Fe_3GeTe_2. Based on our results and physical interpretation, we expect that the interlayer exchange interactions present in other bulk FGT systems would modify the corresponding T_C w.r.t. the monolayer and one can probably expect a linear trend for T_C vs. n similar to experiment.

Next, we investigate $S(\mathbf{k}, \epsilon), D(\epsilon)$, effective mass m^*/m for Fe-d states, Sommerfeld co-efficient[67] for Fe_3GeTe_2 bulk using GGA, GGA + DMFT and compare them with experimental reports. Figure 7 shows DOS for Fe_3GeTe_2 bulk using (a) GGA + DMFT and (b) GGA. DOS obtained using GGA+DMFT is in good agreement with experimental photoemission spectra (PES) as well as previous DMFT results. A slight discrepancy might occur due to different solvers used in the calculations[29]. Using the density of states at Fermi level, we find Sommerfeld co-efficient γ to be 112 and 61 mJ/mol K^2 using GGA + DMFT and GGA, respectively. Note, the GGA+DMFT computed value of γ agrees well the experimental value reported by previous authors[68].

Spectral function $S(\mathbf{k}, \epsilon)$ for bulk Fe_3GeTe_2 along $\overline{K} - \overline{\Gamma} - \overline{K}$ are reported in Fig 8a–c GGA and (d–f) GGA + DMFT. These plots are obtained at different k_z values to understand the contributions coming from different k_z planes to the electronic band structure. Comparing the spectral functions with experimental angle resolved photoemission spectroscopy (ARPES) data reported in refs. [69,70], we find that the electronic structure obtained using GGA +DMFT is in better agreement with experiment. Especially, the features appearing between 0.2 and 0.7 eV below the Fermi level

are in a qualitative agreement with ARPES and previous DMFT calculations[69,70] whereas the GGA band structure is quite far from experiment (both qualitatively and quantitatively).

We calculate the effective mass m^*/m of different Fe-d states of bulk Fe_3GeTe_2 using the following Eq. (11).

$$(m^*/m)_{l\sigma} = \left(1 - \frac{\delta Re\Sigma_{l\sigma}(\omega)}{\delta \omega}\bigg|_{\omega=0}\right), \tag{11}$$

where $Re\Sigma(\omega)$ is real-part of the self-energy with real frequency ω and σ is the electron spin. The value of m^*/m gives a quantitative measurement of electron correlation. Similar to the magnetic moment and exchange interactions, a site dependence is also observed in m^*/m, see Table 3. Fe1 (Fe2) sublattice (magnetic moment = 2.52 μ_B) has smaller effective mass than Fe3 (magnetic moment = 1.31 μ_B), thus implying that the d states of Fe1 are more correlated than Fe3. The spin-resolved m^*/m values decomposed over Fe-d are reported in Table 3 which are in agreement with the quasi-particle mass obtained from experimental ARPES data[69,70] and previous DMFT computed m^*/m for this system[29]. m^*/m for Fe-d states of Fe_nGeTe_2 monolayers are reported in Supplementary Tables 3–4. Comparing m^*/m reported in Table 3 with Supplementary Table 3, we observe that the quasi-particle mass remains almost unchanged between bulk and monolayer. Therefore, the m^*/m values obtained for other Fe_nGeTe_2 monolayers can be considered as a good estimation to determine m^*/m of the corresponding bulk systems.

In summary, we have performed a systematic investigation of the electronic structure and magnetic properties of Fe_nGeTe_4 ($n = 3, 4$, and 5) systems by GGA, LSDA, GGA + U and GGA + DMFT methods. By using the computed parameters in the spin Hamiltonian, the Curie temperature for each FGT monolayer was determined. We discard LSDA to investigate the magnetic interactions and electronic properties of Fe_nGeTe_2 systems since LSDA fails to produce correct unit cell parameters. Based on our results, it is quite evident that, GGA + U with static electronic correlations is not applicable for these systems, since it produces wrong values of lattice parameters, magnetic moments and Curie temperature compared with experiments. We find that the magnetic moments obtained using standard GGA are compatible with the experimental results, but the Curie temperature is overestimated. Upon the inclusion of dynamical electronic correlations within the GGA + DMFT approach, the magnetic moments remain almost unchanged, while the exchange interactions, especially the isotropic symmetric exchange parameters get significantly modified to decrease the Curie temperature
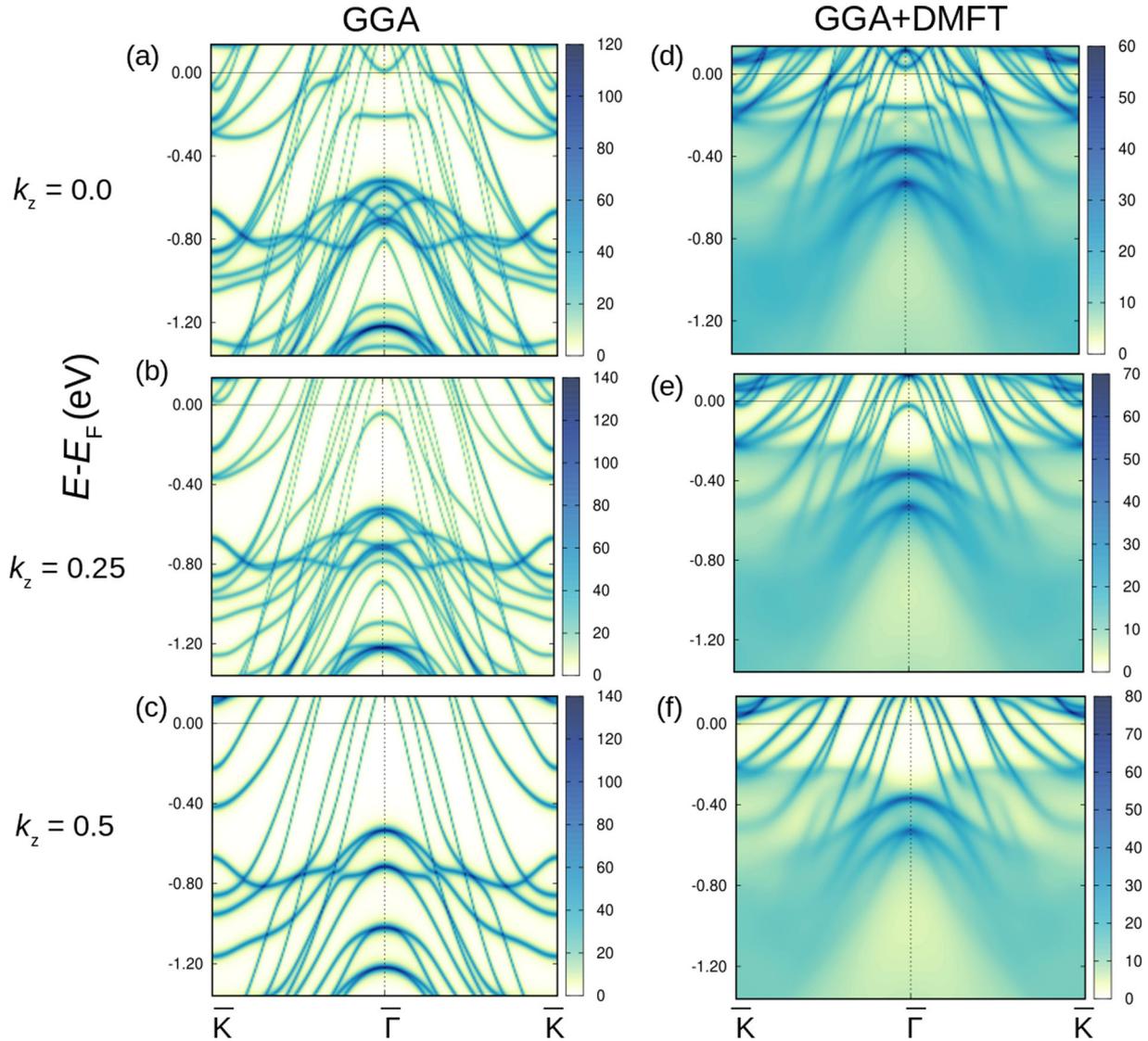
Fig. 8   Spectral function S(k, ϵ) for bulk Fe₃GeTe₂. S(k, ϵ) plotted using (**a**) GGA and (**b**) GGA + DMFT (at T = 150 K).

Table 3.   Effective mass m^*/m for different Fe-d states of Fe₃GeTe₂ bulk.

Species	Orbital	$m^*/m\uparrow$ (Calc.)	$m^*/m\downarrow$ (Calc.)	m^*/m (Expt.)
Fe1	d_{z^2}	2.00	2.08	1.54[88]
	$d_x^2 - y^2$	1.75	2.11	
	d_{yz}	1.78	1.95	
	d_{xz}	1.78	1.95	
	d_{xy}	1.75	2.11	
Fe3	d_{z^2}	1.44	1.78	1.6[69]
	$d_x^2 - y^2$	1.42	1.62	
	d_{yz}	1.55	1.66	
	d_{xz}	1.55	1.66	
	d_{xy}	1.42	1.62	

substantially to have a nice agreement with the experimental results. In addition to the transition temperatures, density of states, band structure and effective mass calculated with GGA + DMFT agree well with previous experiments. This implies that consideration of dynamical correlations is necessary to capture the correct electronic structure and magnetic behavior of the FGT systems.

METHODS

Density functional theory (DFT) based calculations are performed to study the structural, electronic, and magnetic properties of Fe$_n$GeTe₂ (FGT family) systems. Structural optimizations are performed using Vienna Ab initio Simulation Package (VASP)[71,72], where the exchange-correlation potential has been treated with the generalized gradient approximation (GGA), with the Perdew-Burke-Ernzerhof (PBE) functional[73]. Calculations within local spin density approximation (LSDA) are done using Perdew-Zunger functional[74].

We use $18 \times 18 \times 1$ Monkhorst-Pack k-point mesh in our calculations for Brillouin zone (BZ) integration.[75] To model isolated 2D monolayers, the interaction between periodic images of the supercell along the z-axis is reduced by adding a 20 Å vacuum region perpendicular to the surface of monolayers. The lattice constants and atomic coordinates are optimized by minimizing energy based on the conjugate gradient method with a force

component tolerance of 0.01 eV/Å on each atom. The energy cutoff for the plane-wave basis set iss set to 500 eV.

To have more accurate prediction of localized magnetic properties, we used the full-potential linear muffin-tin orbital (FP-LMTO) method, implemented in the RSPt code[40,76]. The k-point grids with dimensions $21 \times 21 \times 1$ and $36 \times 36 \times 1$ are constructed for calculating the magnetic exchange interactions (J_{ij}) and magnetic anisotropy energy (MAE), respectively. Within the scope of FP-LMTO, we study the electronic and magnetic properties of FGT systems using different computational approaches: DFT, dynamical mean-field theory (DMFT) and DFT +U.

DMFT methodology

The key concept of DMFT is that the Hubbard model is mapped locally to an effective Anderson impurity model, where the problem of an entire lattice is converted into the simple problem of an atom embedded in an electronic bath. Each lattice-site is coupled with the bath which represents rest of the crystal and electron on the single site could be created or annihilated by coupling with the electronic bath[38]. The Hamiltonian of the Anderson impurity model can be written as:

$$H_{AIM} = H_{atom} + \sum_{v,\sigma} \epsilon_v a_{v\sigma}^\dagger a_{v\sigma} + \sum_{v\sigma} (V_v c_{0\sigma}^\dagger a_{v\sigma} + h.c.) + U n_{0\uparrow} n_{0\downarrow},$$

(12)

where H_{atom} includes the single site interactions and ϵ_v is the energy associated with the bath electrons. The first two terms can be considered as the non-interaction energy terms. While the third term describes the coupling between the bath electrons and the electron on the single atom site, where V_v is the strength of this coupling. ($c_{0,\sigma}^\dagger, c_{0,\sigma}$) and ($a_{v,\sigma}^\dagger, a_{v,\sigma}$) are the degrees of freedom for the on-site and bath electrons, respectively. The last term describes the local Coulomb interaction U.

The converged DFT calculations are the starting point to perform our DMFT calculations as implemented in RSPt[40,77]. The first step of the DFT + DMFT or DMFT method is to identify a set of local orbitals, which are not properly described by the standard DFT technique. The Hamiltonian written in Eq. (12) can be solved through DMFT, and convergence should be achieved for both the local self-energy and the full electron density. To solve the effective impurity problem arising in the DMFT cycle we use the spin polarized T-matrix fluctuation-exchange (SPTF) solver[40]. SPTF solver is chosen for our calculations due to its efficiency and accuracy for the moderately correlated systems[78,79]. The double counting correction H_{DC} is considered as the orbitally averaged static part of the self-energy, which is usually done for the SPTF solver[78,80]. In our calculations we use full-potential muffin-tin orbitals as implemented in the RSPt code. The effective Hubbard parameter U_{eff} used in our calculations are obtained from the constrained linear response method, as described in the "Results and discussion" section.

Methodology for J_{ij} calculations

The isotropic symmetric exchange interactions J_{ij} are calculated within the full-potential linearized muffin-tin orbital (FPLMTO) basis implemented in the RSPt code. From the LMTO basis, one can construct the Bloch sums to solve the DFT eigenvalue problem and subsequently for the one-electron Green's function. We have considered Löwdin orthonormalized LMTO basis functions, which are not very localized due to their long decaying tail, and are more physical for metallic systems like Fe$_5$GeTe$_2$. For a detailed description of the shape of various local orbitals used in RSPt, please see ref. [61]. The Löwdin orbitals used in our calculations have been constructed from the original LMTO basis functions performing a k-point-wise orthonormalization[61].

J_{ij} can be extracted from the Green's function obtained from the LMTO basis. The generalized expression for the intersite exchange parameters is given by:

$$J_{ij} = \frac{T}{4} \sum_n [\hat{\Delta}_i(i\omega_n)\hat{G}_{ij}^\uparrow \hat{\Delta}_j(i\omega_n)\hat{G}_{ji}^\downarrow],$$

(13)

The most important quantities in this expression are the onsite spin splitting Δ_i and the spin-dependent intersite Green's function $\hat{G}_{ij}$. The trace in Eq. (13) is taken over the orbital degrees of freedom. T and $\omega_n = 2\pi T(2n + 1)$ are the temperature and the nth fermionic Matsubara frequency respectively. Our DMFT simulations are performed at $T = 150$ K. $\hat{G}_{ij}^\sigma$ is the intersite Green's function between sites i and j and projected over a given spin σ. The term Δ_i gives the exchange splitting at site i, obtained using spin and site-projected Kohn-Sham Hamiltonian. In the presence of dynamical electronic correlations, Eq. (13) gets modified and in DMFT the J_{ij} parameters are calculated using Eq. (4) as mentioned in the "Results and discussion" section.

Methodology for D_{ij} calculations

In order to obtain information on more complex magnetic interactions, one has to generalize this approach to the relativistic case, which has been done already within the Korringa-Kohn-Rostoker (KKR) Green-function method[81]. The details concerning the implementation of antisymmetric exchange interactions in RSPt and the calculation results for different correlated systems are discussed in refs. [81] and[82].

Monte Carlo simulations

To estimate the magnetic ordering temperatures, we perform classical Monte Carlo (MC) simulations via UppASD code[83], where the calculated magnetic parameters are implemented in the Hamiltonian introduced in Eq. (3). We assume identical K_i for all Fe sites by averaging the total MAE/cell by the number of Fe atoms present in the unit cell. To achieve properly averaged properties, simulations are performed with varying cell dimensions, imposing periodic boundary conditions along x and y directions. We have checked the convergence of T_C values for Fe$_n$GeTe$_2$ monolayer by increasing the dimension of sample size used in Monte Carlo simulations up to 800×800 Å^2, which is comparable to the system-size used in laboratory experiments, and have found that the transition temperature remains almost unaltered till the maximum cell dimension considered. In the Monte Carlo simulations temperature is varied from 1000 K to 0 K in step of 5 K. For each temperature step 10^6 Monte Carlo cycles are run. The transition temperatures are estimated by monitoring the cross sections of fourth-order cumulants of magnetization.

There are other methods to calculate the transition temperature, for example, re-normalized spin wave theory based calculations[84].

Constrained linear response method

We compute the Hubbard U parameter by means of constrained-density-functional calculations. The Hubbard U is computed by varying the electron occupation of a single site by constructing a supercell where the periodically repeated sites are perturbed coherently. In this supercell approach, the occupation of one representative site in a large cell is changed leaving all other site occupations unchanged.

The effective interaction parameter U associated to site i in terms of the response function χ is given by: $U = (\chi_0^{-1} - \chi^{-1})_{ii}$

We perform a well converged self-consistent field DFT calculation for the unperturbed system for all sites in the supercell. Then starting from its self-consistent potential, small positive and negative potential shifts are added to each nonequivalent

"Hubbard" site j and the variation of the occupations for all the i sites present in the supercell is computed in two steps: (i) re-adjusting the Kohn-Sham potential of the system self-consistently to optimally screen the localized perturbation, and (ii) without allowing this screening. This latter result is nothing but the variation computed from the first iteration in the self-consistent cycle leading eventually to the former (screened) results. The site-occupation derivatives calculated according to (i) and (ii) produce the matrices χ_{ij} and χ_{ij}^0, respectively. The difference between these matrices gives the value of the Hubbard parameter U.

This scheme is rotationally invariant, therefore the Hund's exchange J_{H}, describing these effects can be considered as zero, or the effect of J_{H} can be mimicked by redefining the U parameter as $U_{\mathrm{eff}} = U - J$, which is known as Dudarev scheme in literature[85].

DATA AVAILABILITY
The data supporting the findings of this study are available from the corresponding authors upon request.

CODE AVAILABILITY
Among the codes used for this study, only VASP is commercially available. RSPt and UppASD are in public domain.

REFERENCES
1. Geim, A. K. & Novoselov, K. S. The rise of graphene. *Nat. Mater.* **6**, 183–191 (2007).
2. Mak, K. F., Shan, J. & Ralph, D. C. Probing and controlling magnetic states in 2d layered magnetic materials. *Nat. Rev. Phys.* **1**, 646–661 (2019).
3. Gong, C. et al. Discovery of intrinsic ferromagnetism in two-dimensional van der Waals crystals. *Nature* **546**, 265–269 (2017).
4. Mermin, N. D. & Wagner, H. Absence of ferromagnetism or antiferromagnetism in one-or two-dimensional isotropic Heisenberg models. *Phys. Rev. Lett.* **17**, 1133 (1966).
5. Huang, B. et al. Layer-dependent ferromagnetism in a van der Waals crystal down to the monolayer limit. *Nature* **546**, 270–273 (2017).
6. Xu, C., Feng, J., Xiang, H. & Bellaiche, L. Interplay between Kitaev interaction and single ion anisotropy in ferromagnetic CrI$_3$ and CrGeTe$_3$ monolayers. *npj. Comput. Mater.* **4**, 57 (2018).
7. Cortie, D. L. et al. Two-dimensional magnets: forgotten history and recent progress towards spintronic applications. *Adv. Funct. Mater.* **30**, 1901414 (2020).
8. Žutić, I., Fabian, J. & Sarma, S. D. Spintronics: fundamentals and applications. *Rev. Mod. Phys.* **76**, 323 (2004).
9. Cortie, D. L. et al. Two-dimensional magnets: forgotten history and recent progress towards spintronic applications. *Adv. Funct. Mater* **30**, 1901414 (2020).
10. Gong, C. et al. Discovery of intrinsic ferromagnetism in two-dimensional van der Waals crystals. *Nature* **546**, 265–269 (2017).
11. Bhatti, S. et al. Spintronics based random access memory: a review. *Mater. Today* **20**, 530–548 (2017).
12. Li, X. et al. Spin-dependent transport in van der Waals magnetic tunnel junctions with Fe$_3$GeTe$_2$ electrodes. *Nano Lett.* **19**, 5133–5139 (2019).
13. Huang, K., Shao, D.-F. & Tsymbal, E. Y. Ferroelectric control of magnetic skyrmions in two-dimensional van der Waals heterostructures. *Nano Lett.* **22**, 3349–3355 (2022).
14. Zhang, Y. et al. Ultrathin magnetic 2D single-crystal crse. *Adv. Mater.* **31**, 1900056 (2019).
15. Kang, L. et al. Phase-controllable growth of ultrathin 2d magnetic FeTe crystals. *Nat. Commun.* **11**, 3729 (2020).
16. Wu, H. et al. Strong intrinsic room-temperature ferromagnetism in freestanding non-van der Waals ultrathin 2D crystals. *Nat. Commun.* **12**, 5688 (2021).
17. Meng, L. et al. Anomalous thickness dependence of curie temperature in air-stable two-dimensional ferromagnetic 1T-CrTe$_2$ grown by chemical vapor deposition. *Nat. Commun.* **12**, 809 (2021).
18. Zhao, B. et al. A room-temperature spin-valve with van der Waals ferromagnet Fe$_5$GeTe$_2$/graphene heterostructure. *Adv. Mater* **35**, 2209113 (2023).
19. Zhang, H. et al. Itinerant ferromagnetism in van der Waals Fe$_{5-x}$GeTe$_2$ crystals above room temperature. *Phys. Rev. B* **102**, 064417 (2020).
20. May, A. F. et al. Ferromagnetism near room temperature in the cleavable van der Waals crystal Fe$_5$GeTe$_2$. *ACS Nano* **13**, 4436–4442 (2019).
21. Ly, T. T. et al. Direct observation of fe-ge ordering in Fe$_{5-x}$GeTe$_2$ crystals and resultant helimagnetism. *Adv. Funct. Mater.* **31**, 2009758 (2021).
22. Liu, Q. et al. Layer-dependent magnetic phase diagram in Fe$_n$GeTe$_2$ (3≤ n≤7) ultrathin films. *Commun. Phys.* **5**, 1–10 (2022).
23. Joe, M., Yang, U. & Lee, C. First-principles study of ferromagnetic metal Fe$_5$GeTe$_2$. *N. Mater. Sci.* **1**, 299–303 (2019).
24. Zhuang, H. L., Kent, P. R. C. & Hennig, R. G. Strong anisotropy and magnetostriction in the two-dimensional stoner ferromagnet Fe$_3$GeTe$_2$. *Phys. Rev. B* **93**, 134407 (2016).
25. Clifton, S. E. Collective electron ferromagnetism. *Proc. R. Soc. Lond. Ser. A. Math. Phys. Sci.* **165**, 372–414 (1938).
26. Wang, H. et al. Pressure-dependent intermediate magnetic phase in thin Fe$_3$GeTe$_2$ flakes. *J. Phys. Chem. Lett.* **11**, 7313–7319 (2020).
27. Xu, X. et al. Signature for non-stoner ferromagnetism in the van der Waals ferromagnet Fe$_3$GeTe$_2$. *Phys. Rev. B* **101**, 201104 (2020).
28. Schmitt, M. et al. Skyrmionic spin structures in layered Fe$_5$GeTe$_2$ up to room temperature. *Commun. Phys.* **5**, 254 (2022).
29. Zhu, J.-X. et al. Electronic correlation and magnetism in the ferromagnetic metal Fe$_3$GeTe$_2$. *Phys. Rev. B* **93**, 144404 (2016).
30. Seo, J. et al. Nearly room temperature ferromagnetism in a magnetic metal-rich van der Waals metal. *Sci. Adv.* **6**, 8912 (2020).
31. Ershadrad, S., Ghosh, S., Wang, D., Kvashnin, Y. & Sanyal, B. Unusual magnetic features in two-dimensional Fe$_5$GeTe$_2$ induced by structural reconstructions. *J. Phys. Chem. Lett.* **13**, 4877–4883 (2022).
32. Kim, D., Lee, C., Jang, B. G., Kim, K. & Shim, J. H. Drastic change of magnetic anisotropy in Fe$_3$GeTe$_2$ and Fe$_4$GeTe$_2$ monolayers under electric field studied by density functional theory. *Sci. Rep.* **11**, 17567 (2021).
33. May, A. F., Du, M.-H., Cooper, V. R. & McGuire, M. A. Tuning magnetic order in the van der Waals metal Fe$_5$GeTe$_2$ by cobalt substitution. *Phys. Rev. Mater.* **4**, 074008 (2020).
34. Cococcioni, M. & de Gironcoli, S. Linear response approach to the calculation of the effective interaction parameters in the LDA+U method. *Phys. Rev. B* **71**, 035105 (2005).
35. Shen, Z.-X., Bo, X., Cao, K., Wan, X. & He, L. Magnetic ground state and electron-doping tuning of curie temperature in Fe$_3$GeTe$_2$: First-principles studies. *Phys. Rev. B* **103**, 085102 (2021).
36. May, A. F., Calder, S., Cantoni, C., Cao, H. & McGuire, M. A. Magnetic structure and phase stability of the van der Waals bonded ferromagnet Fe$_{3-x}$GeTe$_2$. *Phys. Rev. B* **93**, 014411 (2016).
37. Verchenko, V. Y., Tsirlin, A. A., Sobolev, A. V., Presniakov, I. A. & Shevelkov, A. V. Ferromagnetic order, strong magnetocrystalline anisotropy, and magnetocaloric effect in the layered telluride Fe$_{3-\delta}$GeTe$_2$. *Inorg. Chem.* **54**, 8598–8607 (2015).
38. Georges, A., Kotliar, G., Krauth, W. & Rozenberg, M. J. Dynamical mean-field theory of strongly correlated fermion systems and the limit of infinite dimensions. *Rev. Mod. Phys.* **68**, 13–125 (1996).
39. Pourovskii, L. V., Katsnelson, M. I. & Lichtenstein, A. I. Correlation effects in electronic structure of actinide monochalcogenides. *Phys. Rev. B* **72**, 115106 (2005).
40. Wills, J., Eriksson, O., Alouani, M. & Price, D. *Full-Potential LMTO Total Energy and Force Calculations* (Springer Berlin Heidelberg, Berlin, Heidelberg, 2000).
41. Georges, A., Kotliar, G., Krauth, W. & Rozenberg, M. J. Dynamical mean-field theory of strongly correlated fermion systems and the limit of infinite dimensions. *Rev. Mod. Phys.* **68**, 13–125 (1996).
42. Turkowski, V., Kabir, A., Nayyar, N. & Rahman, T. S. Dynamical mean-field theory for molecules and nanostructures. *J. Chem. Phys.* **136**, 114108 (2012).
43. Kim, T. J., Ryee, S., Han, M. J. & Choi, S. Dynamical mean-field study of vanadium diselenide monolayer ferromagnetism. *2D Mater.* **7**, 035023 (2020).
44. Zhou, Z., Pandey, S. K. & Feng, J. Dynamical correlation enhanced orbital magnetization in VI$_3$. *Phys. Rev. B* **103**, 035137 (2021).
45. Kvashnin, Y. O., Rudenko, A. N., Thunström, P., Rösner, M. & Katsnelson, M. I. Dynamical correlations in single-layer CrI$_3$. *Phys. Rev. B* **105**, 205124 (2022).
46. Hu, X. et al. Enhanced ferromagnetism and tunable magnetism in Fe$_3$GeTe$_2$ monolayer by strain engineering. *ACS Appl. Mater. Interfaces* **12**, 26367–26373 (2020).
47. Zhao, M. et al. Kondo holes in the two-dimensional itinerant ising ferromagnet Fe$_3$GeTe$_2$. *Nano Lett.* **21**, 6117–6123 (2021).
48. Zhang, Y. et al. Emergence of kondo lattice behavior in a van der Waals itinerant ferromagnet, Fe$_3$GeTe$_2$. *Sci. Adv.* **4**, eaao6791 (2018).
49. Kim, T. J., Ryee, S. & Han, M. J. Fe$_3$GeTe$_2$: a site-differentiated hund metal. *npj Comput. Mater.* **8**, 245 (2022).
50. Chen, X. et al. Pervasive beyond room-temperature ferromagnetism in a doped van der Waals magnet. *Phys. Rev. Lett.* **128**, 217203 (2022).
51. Fedorova, N. S., Ederer, C., Spaldin, N. A. & Scaramucci, A. Biquadratic and ring exchange interactions in orthorhombic perovskite manganites. *Phys. Rev. B* **91**, 165122 (2015).

52. Yang, X., Zhou, X., Feng, W. & Yao, Y. Strong magneto-optical effect and anomalous transport in the two-dimensional van der Waals magnets Fe_nGeTe_2 ($n = 3, 4, 5$). *Phys. Rev. B* **104**, 104427 (2021).

53. Li, D., Smogunov, A., Barreteau, C., Ducastelle, Fmc & Spanjaard, D. Magnetocrystalline anisotropy energy of Fe (001) and Fe (110) slabs and nanoclusters: a detailed local analysis within a tight-binding model. *Phys. Rev. B* **88**, 214413 (2013).

54. Jenkins, S. et al. Breaking through the mermin-wagner limit in 2d van der Waals magnets. *Nat. Commun.* **13**, 6917 (2022).

55. Li, Z. et al. Magnetic critical behavior of the van der Waals Fe_5GeTe_2 crystal with near room temperature ferromagnetism. *Sci. Rep.* **10**, 15345 (2020).

56. Fei, Z. et al. Two-dimensional itinerant ferromagnetism in atomically thin Fe_3GeTe_2. *Nat. Mater.* **17**, 778–782 (2018).

57. Roemer, R., Liu, C. & Zou, K. Robust ferromagnetism in wafer-scale monolayer and multilayer Fe_3GeTe_2. *npj 2D Mater. Appl.* **4**, 2397–7132 (2020).

58. Chakraborty, A. et al. Magnetic skyrmions in a thickness tunable 2D ferromagnet from a defect driven dzyaloshinskii-moriya interaction. *Adv. Mater.* **34**, 2108637 (2022).

59. Mayoh, D. A. et al. Effects of fe deficiency and co substitution in polycrystalline and single crystals of Fe_3GeTe_2. *Cryst. Growth Des.* **21**, 6786–6792 (2021).

60. Yi, J. et al. Competing antiferromagnetism in a quasi-2D itinerant ferromagnet: Fe_3GeTe_2. *2D Mater.* **4**, 011005 (2016).

61. Kvashnin, Y. O. et al. Exchange parameters of strongly correlated materials: extraction from spin-polarized density functional theory plus dynamical mean-field theory. *Phys. Rev. B* **91**, 125133 (2015).

62. Borisov, V. et al. Tuning skyrmions in B20 compounds by 4d and 5d doping. *Phys. Rev. Mater.* **6**, 084401 (2022).

63. Liechtenstein, A. I., Katsnelson, M. I., Antropov, V. P. & Gubanov, V. A. Local spin density functional approach to the theory of exchange interactions in ferromagnetic metals and alloys. *J. Magn. Magn. Mater.* **67**, 65–74 (1987).

64. Kim, D. et al. Antiferromagnetic coupling of van der Waals ferromagnetic Fe_3GeTe_2. *Nanotechnology* **30**, 245701 (2019).

65. Jang, S. W. et al. Origin of ferromagnetism and the effect of doping on Fe_3GeTe_2. *Nanoscale* **12**, 13501–13506 (2020).

66. Zhu, M. et al. Strain modulation of magnetic coupling in the metallic van der Waals magnet Fe_3GeTe_2. *Intermetallics* **131**, 107085 (2021).

67. Ashcroft, N. W. & Mermin, N. D. *Solid Sate Physics* (Holt-Saunders, Saunders College, Philadelphia, 1976).

68. Liu, Y., Stavitski, E., Attenkofer, K. & Petrovic, C. Anomalous hall effect in the van der Waals bonded ferromagnet $Fe_{3−x}GeTe_2$. *Phys. Rev. B* **97**, 165415 (2018).

69. Xu, X. et al. Signature for non-stoner ferromagnetism in the van der Waals ferromagnet Fe_3GeTe_2. *Phys. Rev. B* **101**, 201104 (2020).

70. Deng, Y. et al. Gate-tunable room-temperature ferromagnetism in two-dimensional Fe_3GeTe_2. *Nature* **563**, 94–99 (2018).

71. Kresse, G. & Joubert, D. From ultrasoft pseudopotentials to the projector augmented-wave method. *Phys. Rev. B* **59**, 1758 (1999).

72. Kresse, G. & Hafner, J. Norm-conserving and ultrasoft pseudopotentials for first-row and transition elements. *J. Phys. Condens. Matter* **6**, 8245 (1994).

73. Perdew, J. P., Burke, K. & Ernzerhof, M. Generalized gradient approximation made simple. *Phys. Rev. Lett.* **77**, 3865 (1996).

74. Perdew, J. P. & Zunger, A. Self-interaction correction to density-functional approximations for many-electron systems. *Phys. Rev. B* **23**, 5048–5079 (1981).

75. Monkhorst, H. J. & Pack, J. D. Special points for brillouin-zone integrations. *Phys. Rev. B* **13**, 5188 (1976).

76. Wills, J. M. & Cooper, B. R. Synthesis of band and model hamiltonian theory for hybridizing cerium systems. *Phys. Rev. B* **36**, 3809–3823 (1987).

77. Grånäs, O. et al. Charge self-consistent dynamical mean-field theory based on the full-potential linear muffin-tin orbital method: methodology and applications. *Comput. Mater. Sci.* **55**, 295–302 (2012).

78. Grechnev, A. et al. Theory of bulk and surface quasiparticle spectra for Fe, Co, and Ni. *Phys. Rev. B* **76**, 035107 (2007).

79. Pourovskii, L. V., Katsnelson, M. I. & Lichtenstein, A. I. Correlation effects in electronic structure of actinide monochalcogenides. *Phys. Rev. B* **72**, 115106 (2005).

80. Lichtenstein, A. I., Katsnelson, M. I. & Kotliar, G. Finite-temperature magnetism of transition metals: An ab initio dynamical mean-field theory. *Phys. Rev. Lett.* **87**, 067205 (2001).

81. Kvashnin, Y. O., Bergman, A., Lichtenstein, A. I. & Katsnelson, M. I. Relativistic exchange interactions in CrX_3 ($X = $ Cl, Br, I) monolayers. *Phys. Rev. B* **102**, 115162 (2020).

82. Borisov, V. et al. Heisenberg and anisotropic exchange interactions in magnetic materials with correlated electronic structure and significant spin-orbit coupling. *Phys. Rev. B* **103**, 174422 (2021).

83. Eriksson, O., Bergman, A., Bergqvist, L. & Hellsvik, J. *Atomistic Spin Dynamics: Foundations and Applications* (Oxford University Press, 2017).

84. Li, Z., Cao, T. & Louie, S. G. Two-dimensional ferromagnetism in few-layer van der Waals crystals: Renormalized spin-wave theory and calculations. *J. Magn. Magn. Mater.* **463**, 28–35 (2018).

85. Dudarev, S. L., Botton, G. A., Savrasov, S. Y., Humphreys, C. J. & Sutton, A. P. Electron-energy-loss spectra and the structural stability of nickel oxide: an LSDA +U study. *Phys. Rev. B* **57**, 1505–1509 (1998).

86. Chen, B. et al. Magnetic properties of layered itinerant electron ferromagnet Fe_3GeTe_2. *J. Phys. Soc. Jpn.* **82**, 124711 (2013).

87. Ribeiro, M. et al. Large-scale epitaxy of two-dimensional van der Waals room-temperature ferromagnet Fe_5GeTe_2. *npj 2D Mater. Appl.* **6**, 10 (2022).

88. Kim, K. et al. Large anomalous hall current induced by topological nodal lines in a ferromagnetic van der Waals semimetal. *Nat. Mater.* **17**, 794–799 (2018).

AUTHOR CONTRIBUTIONS

S.G. carried out the calculations. All authors discussed the results and co-wrote the paper.

COMPETING INTERESTS

The authors declare no competing interests.

ADDITIONAL INFORMATION

Supplementary information The online version contains supplementary material available at https://doi.org/10.1038/s41524-023-01024-5.

Correspondence and requests for materials should be addressed to Biplab Sanyal.

Reprints and permission information is available at http://www.nature.com/reprints

Publisher's note Springer Nature remains neutral with regard to jurisdictional claims in published maps and institutional affiliations.